

Remote Sensing of Mauna Loa

Anne B. Kahle¹, Michael J. Abrams¹, Elsa A. Abbott¹, Peter J. Mouginis-Mark², and Vincent J.

Realmuto¹

¹*Jet Propulsion Laboratory, California Institute of Technology, Pasadena, California*

²*University of Hawaii, Honolulu, Hawaii*

The application of remote sensing to the study of volcanoes has advanced considerably in recent years. The availability of digital multispectral data, acquired from satellite or airborne instruments, has allowed us to infer many properties of the surface material. Each wavelength region offers specific information relating to the chemical and physical state of eruptive products. The reflected visible through thermal part of the spectrum reveals information relating to iron oxidation state, vegetation cover, development of silica coatings, and presence of SO₂, among others. The microwave part of the spectrum reveals information relating to surface roughness and dielectric constant variations. The use of these data to study and map volcanoes can save time and effort for mapping; and can greatly reduce the risk associated with doing fieldwork on active volcanoes. Satellite instruments due to be launched in the next five years promise to provide far better data than are currently available from space.

1. INTRODUCTION

Remote sensing is proving to be a valuable tool for studying volcanoes. Large areas can be observed rapidly, safely, and, if using satellites, frequently. In addition to providing images (sometimes stereoscopic) comparable to aerial photographs and amenable to the traditional photographic interpretation, remote sensing instrumentation generally provides multispectral data in digital format. From these data, we can infer many properties of the surface material. In this chapter, we will discuss remote sensing at visible, infrared and microwave wavelengths. There have been some satellite observations of Mauna Loa and the island of Hawaii with the Advanced Very High Resolution Radiometer (AVHRR), Japanese Earth Remote Sensing (JERS-1), Landsat, and French Societe Propriete d'Observation de la Terre (SPOT) satellites and with Shuttle imaging Radar (SIR-B and SIR-C) (see, for example, the cover image depicting the Island of Hawaii using SPOT satellite data combined with digital elevation; Chadwick, et al., personal communication). However, the most detailed studies have utilized NASA airborne sensors. We will emphasize these latter studies here, as they best demonstrate the potential of the techniques.

In section 2, we discuss the spectral characteristics of materials on the surface of Mauna Loa. In section 3, we show examples of multispectral remotely sensed data in the visible through infrared wavelength regions; in section 4, we discuss remote sensing of SO₂ plumes using thermal infrared (TIR) data; in section 5 we discuss the use of multispectral data for temperature determination; section 6 deals with radar remote sensing; and finally, in section 7, we discuss future remote sensing of Mauna Loa. Figure 1 is

an index map showing the locations of the images that will be discussed in this paper,

2. EVOLUTION OF SPECTRAL FEATURES

2.1. *Introduction: Spectral basis for mapping from remote sensing data*

The surface weathering of Mauna Loa basalts is evidenced by distinct chemical and mechanical changes, beginning during initial cooling. These changes have been used to estimate the relative ages of individual flows [Kahle, et al., 1988; Abram, et al., 1991] from remote sensing data in both the visible to short wavelength infrared (SWIR) region (0.5–2.4 μm) and part of the thermal infrared (TIR) region (8–12 μm).

On the windward side of the island of Hawaii and in other humid areas, vegetation growth is so rapid that lava surfaces are obscured from aerial view in a very few years. In contrast, lava flows in arid regions on the island are nearly unvegetated and may remain barren for long periods of time. During this interval, the change most obvious to the eye is the oxidation of iron, so that the surface, originally black or dark brown, becomes reddish or tan [Lockwood and Lipman, 1987]. Other less obvious changes also occur, including the accretion of silica-rich veneers or coatings (~80 wt% SiO_2) derived largely from windblown soil [Curtiss, et al., 1985] or tephra [Farr and Adams, 1984] and the devitrification of the thin (~50 μm) glassy crusts or chill coats so common on fresh pahoehoe. The coats may also spall to reveal a more vesicular crystalline substrate. While the flows are still active and during cooling, acid aerosols in the vicinity of gases escaping from the melt can cause chemical changes to the already emplaced rock, leaching out iron and other cations, and leaving a more silica-rich rock. In addition, mechanical weathering of the flows encourages colonization by vegetation; very old flows in kipukas, for example, tend to be heavily vegetated. The effects of these and other processes on the spectral characteristics of weathering lava flows will be discussed in more detail in the next sections. We will also show how it has been possible to capitalize on these spectral changes to determine relative age relations of lava flows on Mauna Loa.

2.2. *Visible to short wavelength infrared region*

The spectrum of basalt in the visible to short wavelength infrared (0.4–2.4 μm) region is dominated by the presence of iron in its various oxidation states and by the presence of vegetation. Laboratory measurements of flows of different ages illustrate the effects of iron oxidation on the spectral behavior.

Fresh aa and pahoehoe flows are both nearly flat spectrally and have very low albedo throughout the reflectance part of the spectrum (Figure 2). Pahoehoe can be very smooth and flat and can exhibit strong specular reflection. Laboratory studies were done on samples of basalts col-

lected from an area on the north slope of Mauna I AM [Abrams, et al., 1991]. With increasing age, the overall reflectance increases (from 5-7% to about 12%) for flows up to about 4000 years old. At the same time, there develops a fall-off in reflectance at the blue end ($\sim 0.4 \mu\text{m}$) of the spectrum that becomes progressively more pronounced with age. They attributed both of these effects to the conversion of ferrous iron to ferric iron by oxidation [Hunt, 1977]. Chemical analyses of the samples were done to measure the ferric iron content of the rocks. There is a systematic increase with age of ferric iron, from 3.2% to 4.6%, which correlates with the observed spectral characteristics. The slope of the reflectance curves between 0.8 and $0.4 \mu\text{m}$ is therefore a good measure of the increase in ferric iron content, and hence is correlated to increasing age.

Vegetation cover on Mauna Loa basalts varies as a function of age, rainfall and elevation. Historic flows are essentially unvegetated at higher elevation due to the lack of soil development. Lower down, in areas of heavy rainfall, lichen can begin to grow, especially on the rougher aa, within 2-3 years. Lichen grows early on these flows and after time is replaced by other types of vegetation. At an elevation level of about 2100 meters, flows whose C-14 ages are between 200 and 1500 years have only a few percent cover of shrubs and grasses; flows with C-14 ages between 1500 and 4000 have 5-15% cover; flows older than 4000 years old become heavily vegetated and extensively weathered. The spectrum of healthy vegetation (Figure 2) shows the presence of chlorophyll absorption bands near $0.65 \mu\text{m}$ and $0.45 \mu\text{m}$, a relative high in reflectance near $0.55 \mu\text{m}$ (the reason vegetation is green to the eye), and very high reflectance starting at $0.76 \mu\text{m}$, gradually decreasing towards longer wavelength due to the effects of water absorption bands.

The distinct, and systematic effects of both oxidation and increasing vegetation cover with age on the spectral reflectance characteristics have been exploited to map some of the older lava flows at middle elevations on Mauna Loa, and to determine the relative ages of the older flows. The technique has been shown to be in excellent agreement with standard field mapping techniques [Abrams, et al., 1991].

2.3. Thermal infrared region

The TIR spectral characteristics of basalts are controlled by macroscopic properties, such as the amount and size of vesiculation; by differences related to the Si-O bonding which are in turn related to the silica content; and by chemical alteration of the surfaces from acidic gases. Each of these effects will be discussed with regard to our ability to use these spectral differences to map Mauna Loa flows in the TIR wavelength region.

The thermal infrared radiance emitted from a surface is a function of the temperature and spectral emittance, where the emittance is the parameter related to the composition of the material. For a perfect blackbody, the emittance is unity, and the radiance is strictly a function of the tempera-

ture and wavelength, as described by Planck's Law. Most geologic materials have non-unity emittance at some wavelengths in the TIR; it is this deviation from unity that allows separation and identification of mineral composition. Compared to the visible/near-infrared spectra, the thermal infrared reflectance spectra of the younger basalts show prominent spectral differences. These spectral features are related to Si-O bonding, and facilitate the distinction of different lava flows.

Crisp et al. [1990] investigated the relationship between changes in spectral emittance features and mineralogy of Hawaiian basalts. They collected samples of molten pahoehoe lava from active effusions of Puu Oo in May 1989. The spectra of these fresh samples (after cooling into a glass) exhibit a broad feature peaked between 10.3 and 10.5 μm , indicative of a strong degree of disorder (Figure 3). Disordered glass is made up of silicate units with a wide variety of bond angles, bond strengths, and bonding arrangements that vibrate at different frequencies resulting in broad spectral features in the infrared [e.g., Simon and McMahon, 1953; Brawer and White, 1975; Dowty 1987]. The spectra of the fresh Hawaiian basalts are almost identical to the spectra of samples from older (prehistoric, 1972, 1880, 1899, and 1984) Mauna Loa basaltic lavas that were fused in an oven and quenched [e.g., Kahle, et al., 1988, Figure 3b]. They also closely match the spectra of the glassy interior of older basalts. The persistence of this broad spectral feature in the glassy interior of rocks, even in rocks over 4000 years old, shows how well the interior glass can be protected from weathering processes and can retain its original composition and degree of disorder.

However, as the Hawaiian rocks age and weather, the spectral character of their outer surfaces changes. The first change evident in the spectra of the Hawaiian rocks is that the single broad feature splits into two features that Kahle et al. [1988] and Crisp et al. [1990] call "B" at 9.2–9.5 μm and "C" at 10.5–10.8 μm (Figure 4). After just a few days or weeks of exposure to the elements (rain, atmosphere, and acidic volcanic fumes) the B and C features are evident in some, but not all, of the exposed surfaces. Features B and C are commonly found on the rapidly cooled top surface of flows, but also appear in the interiors when rocks were broken after emplacement and cooling and these interiors were then exposed to the Hawaiian environment for a sufficient time. In samples that they examined that were only a week old, the C feature was always stronger than the B feature.

With increasing age the overall trend is for the B feature to strengthen relative to the C feature. A simple explanation for the evolution of these two emission peaks in the top surfaces of Hawaiian rocks is that the structure of the metastable glass is becoming more ordered with time. Immediately after its rapid quenching in air, the glass is strongly disordered. With time this unstable configuration breaks down and the silica tetrahedra become organized into silica tetrahedral sheetlike (B feature) and chainlike units (C feature) [e.g., Brawer and White, 1975]. With more

time the sheetlike units become the preferred mode. This could be an isochemical process in which the glass structure becomes more ordered by chain units progressively converting to sheet units, or it could be a structural change accompanying a compositional change at the surface.

With continued aging, the height of the C feature decreases until it is undetectable. It is likely that the C feature disappears as the glass becomes more ordered, without any chemical change in the glass. Soon after the B feature overtakes the C feature in height, a new feature they call "A" can appear at about 8.1 or 8.2 μm . The A feature is commonly a shoulder on the side of the B feature. It is very common for samples greater than 50 years old to show an A feature. The A feature has not been found in the week-old samples from Puu Oo but does appear in some samples of the 1984 Mauna Loa flow collected three years after emplacement but only at locations that receive Inert' than 250 cm rainfall per year and in Puu Oo flows 1-5 years after emplacement. Kahle et al. [1988] proposed that the A feature results from the addition of a silica-rich coating. Farr and Adams [1984] describe the development of this coating as the accumulation and leaching of windblown tephra and dust. A scanning electron microscope (SE-M) and thin section investigation [Crisp et al., 1990] of Mauna Loa 1984 samples confirmed that the A feature is associated with a silica-rich rind that appears to be the results of addition of material to the basalt surface rather than leaching of the substrate basalt. Previously, the shortest time documented for the formation of a silica coating was 13 years in an area southwest of Kilauea where the rainfall rate is about 150 cm/year [Farr and Adams, 1984]. As the lava ages further, the spectral contrast decreases slowly until, after a few hundred years, most of the units appear spectrally flat in the infrared. However, as noted in section 2.2, at this time the spectral contrast in the VIS and SWIR becomes more evident.

The spectral character of aa in the thermal infrared is partially controlled by the texture of the material. Radiation emitted by the aa is often partially trapped by the roughness of the surface, which tends to act like a large number of blackbody cavities. However, the spectral signature, while reduced, has features very much like those of similar age pahoehoe. Figure 5 shows lab spectra of aa and pahoehoe of the same age, which have been normalized to the same scale.

Vegetation spectra are essentially equal to blackbody spectra, so the addition of vegetation to the surface serves to reduce the spectral contrast of the materials.

Another influence on the TIR spectral characteristics of basalts is alteration associated with fumarolic activity. Near active venting areas and areas undergoing degassing, hydrous, silica-rich areas form, accompanied by the deposition of sulfate salts [Realmuto, et al., 1992]. This is thought to be caused by acid-leaching of cations by aerosols, and resulting enrichment of silica. The spectral characteristics of this material resemble those produced by the secondary silica coatings described by Crisp et al.

[1990].

3. MAPPING USING REMOTELY SENSED DATA

NASA's Thermal Infrared Multispectral Scanner (TIMS) and the NS001 scanner (a Thematic Mapper simulator) were flown aboard a NASA C-130 aircraft over the island of Hawaii during, November, 1985 at about 1100 local time. TIMS acquires digital radiance data in image format. There are six spectral channels of data between 8 and 12 μm (table 1) [Palluconi and Meeks, 1985]. The sensitivity is 0.1–0.5K. Images are acquired using a mirror that scans an arc of $+38^\circ$ to -38° about nadir, with an angular resolution of 2.5 mrad. The NS001 acquires eight channels of data in the visible, reflected infrared, and thermal infrared parts of the spectrum (table 1). Images are acquired with a scan angle of 100° , and an angular resolution of 2.5 mrad. The C-130 operates at altitudes up to 7.7 km above sea level; thus, the scanners acquire data with a nadir ground pixel size of 25 m or less. For these data flights, the aircraft operated at an altitude of 13.5 km above terrain, producing 8 m pixels.

Digital data from TIMS bands 1, 3 and 5 were processed using a decorrelation stretch algorithm [Gillespie, et al., 1986]. This procedure exaggerates subtle color differences in image data by increasing the saturation and intensity while generally preserving the hue information. Thus, the resulting images can be related back to the spectral information of the components used to create the color triplet image. Because the decorrelation stretch depends upon the frequency distribution of radiance values within the particular image being stretched, colors of the same materials generally vary slightly from image to image.

Figure 6 shows a decorrelation-stretched image of basalt flows on the north flank of Mauna Loa, where TIMS bands 1, 3, and 5 are displayed in blue, green, and red respectively. (The road running diagonally across the image is the Hilo-Kona jeep [rail.]) Despite the chemical and petrologic similarity of the unweathered basalts, Figure 6 shows a wide range of different thermal IR "colors", both within and among the numerous individual lava flows.

Field checking of these and other Hawaiian TIMS images and comparison with geologic maps [Holcomb, 1987; Lockwood, et al., 1988; Lockwood, unpublished data] reveal systematic relationships between the TIMS colors and the type of basalt (pahoehoe or aa) and degree of weathering and, hence, age. Pahoehoe and aa flows are consistently separable in the images where there is little or no vegetation. Single basalt flows of either type may show some image color differences even immediately after eruption [Realmuto, et al., 1992]; however, the greatest color differences appear to be related to age.

Figure 7 is a field-derived geologic map of the same area as Figure 6 for comparison. The contacts of some flows are more accurately portrayed in the images. In a few cases, geologic relations that were difficult to map in the field can easily be seen in the images. One example of this is the boundary between the 1843 (red) and 1935 (blue)

pahoehoe flows, which is difficult to distinguish in the field, but is very distinct in the TMS image.

Freshly broken and unweathered basaltic cinders and crushed basalt exposed in quarries consistently appear cyan or light blue-green in the false-color pictures. In contrast, young aa flows appear dark blue-green, and this color shifts to dark brown or orange with increasing age. The oldest flows are heavily vegetated and appear dark green. In the false-color pictures these flows are not always easy to distinguish from young, largely unvegetated aa. However, they may be separated by temperature. In Figure 6, lightly vegetated aa flows ranged in surface temperature from 35° to 43°C; heavily vegetated flows were ~29°C.

Unvegetated pahoehoe was warmer than aa. Surface temperatures for pahoehoe in Figure 6 ranged from 43° to 54°C.

There is a pronounced and systematic color change with increasing age of pahoehoe. The TMS color shifts from dominantly blue to purple and magenta (compare, for instance, the 1935 and 1880 flows in Figure 6). This range of colors mimics the range for the different initial states. Increasingly older flows show colors not observed for young flows: red (1843) and orange (0.2 --- 1.5 ka), mixed orange and green (1.5 --- 4 ka), and ultimately light green (4 --- 8 ka). The oldest lavas (>8 ka) are forested and appear dark green. Heavily vegetated aa and pahoehoe are probably indistinguishable from each other.

Because of the known color assignments of the TMS wavelength bands, and by comparison with spectra of samples collected in the field, we can relate the colors in the images to the spectral features observed in Figure 4. Spectral feature C is associated with the blue color in the image and A with red. As spectral feature A appears and increases and while feature C diminishes, the colors move progressively from blue to magenta to red. Finally, as the spectral contrast diminishes, the units on the images become green — which here corresponds to spectrally flat.

For aa, young rough flows are associated with dark blue-green TMS colors and very weak spectral features, including subdued B and even some C. Because aa and pahoehoe of the same flow have essentially identical compositions, we attribute the subdued spectrum of the aa to multiple scattering in the rough surface (cavity or black-body radiation). The dark colors in the images are due to low temperatures in the shadowed portions of the rough surface, not yet warmed by the sun at the time (-1 100 LT) of data acquisition.

The shift to brown image color with increasing age of aa is directly caused by the silica-rich rinds. The increased color saturation of these flows is attributed to filling of small cavities with the thermally opaque silica, thereby reducing the amount of blackbody radiation. There is no very old unvegetated aa in the study area. The color of the oldest aa flows in Figure 6 is controlled by the admixture of vegetation, which consistently appears dark green in the false-color images.

Abrams et al. [1991] analyzed the NS00 1 visible and SWIR data for roughly the same area as Figure 6,

separately and also combined with the TIR data. The NS001 data were processed by using Karhunen-Loeve or principal components transformations. This is a dimension reduction procedure that forms linear combinations of the original data based on the variance-covariance matrix [Gillespie, 1980]. The resulting image (Figure 8) depicts the flows in various colors; the overlain interpretation map delineates flow boundaries recognized from the image. On the image, the young pahoehoe flows (1935, 1843, X) 0-500 years old and 500-1500 years old) are all displayed as indistinguishable blue colored units, in contrast with the TIMS image (Figure 9) which allowed easy separation of these units. They are labeled p (pahoehoe) and Op (older pahoehoe) to indicate that they were not differentiable. These flows are still very dark and fresh-looking in the field, and they have not as yet developed significant oxidation of mafic minerals. Spectrally, they are all dark and show no distinguishing features. Older pahoehoe flows become greener on the image, and the oldest, with vegetation cover, are magenta. The aa flows progress from reddish-brown (1935) to brown (1899) to light brown (1843) to blue-brown (200-500 years old) to light blue-green (500-1500 years old) to green-yellow (1500-4000 years old) to dark green (>4000 years old). The relations between the image colors and the increase in iron oxidation and change in reflectance spectra are consistent.

When both data sets are combined by principal components analysis, it was shown that emittance and reflectance spectral properties of the rocks were correlated to some degree, as would be expected. In Figure 10, Abrams et al. [1991] were able to separate by color all of the previously mapped units (Figure 11) and to show systematic color changes, related to relative ages.

These results show the utility of remote sensing in the relative dating of similar basalts in an arid environment, using combined data from the reflectance and emittance parts of the spectrum. The existence of weathering systematics implies that it may prove possible to estimate flow age from remotely sensed data, provided that progression of colors has already been calibrated for a given region. Important influences on the thermal spectra appear to be surface texture, physical and chemical degradation of glassy crusts (spalling, devitrification, alteration), accretion of silica-rich coats, and vegetation growth. Important influences on the reflectance spectra appear to be development of iron oxide minerals from weathering, vegetation growth, and surface texture. At least for the north flank of Mauna Lea, these effects occur in characteristic sequences and at different rates, so that color pictures created from visible to thermal infrared data depict flows at different stages of their development in different colors. The combined use of data in the two wavelength regions provides more information than the use of either separately. These relationships should prove useful in reconnaissance geologic mapping in volcanic fields in other arid or semiarid areas.

4. REMOTE SENSING OF VOLCANIC SO₂ PLUMES

The absorption spectrum of the sulfur dioxide (SO_2) molecule exhibits ultraviolet (UV), infrared (IR), and microwave bands [but are amenable to remote sensing techniques]. All three of these absorption features have been used to measure SO_2 with passive ground-based, airborne, and spaceborne instruments.

Dispersive correlation spectroscopy became the first remote sensing technique to be widely applied to the study of volcanic plumes [cf Stoiber et al., 1983] using the portable correlation spectrometer, or COSPEC [Moffat and Millán, 1971]. COSPEC instruments convert measurements of the UV radiation transmitted through a volcanic plume into estimates of its SO_2 burden [Hamilton et al., 1978; Hoff and Millán, 1981]. The collection of COSPEC measurements at volcanoes throughout the world has allowed volcanologists to estimate the annual volcanic contribution to the global atmospheric SO_2 budget [cf Berresheim and Jaeschke, 1983; Stoiber et al., 1987] and recognize that a rapid change in the SO_2 flux from a volcano can signal an eruption [i.e., Casadevall et al., 1981; Chartier et al., 1988; Malinconico, 1979, 1987; Caltabiano et al., 1994].

A correlation spectrometer can measure only a small portion of a plume; operators must either move the instrument in traverses beneath plumes or occupy locations near vents and pan the instrument across plumes. Wind speed must be measured or known from other sources. The estimation of SO_2 flux rates or spatial and temporal variations in SO_2 contents of volcanic plumes can therefore involve considerable labor, logistical planning, and in some cases, personal risk.

Satellite-based remote sensing techniques, employing the instruments such as the Total Ozone Mapping Spectrometer (TOMS) or the Microwave Limb Sounder (MLS), are largely free of the limitations imposed by field logistics and hazards. A major advance in the remote sensing of volcanicogenic SO_2 occurred in 1983, when Krueger demonstrated that the SO_2 clouds from the eruption of El Chichón could be imaged, or mapped at a 50 km spatial resolution at nadir by TOMS [Krueger, 1983]. TOMS data have since been used to map the SO_2 clouds produced by the recent eruption of Mauna Loa [Casadevall et al., 1984], Nevado del Ruiz [Krueger et al., 1990], Cerro Hudson [Doiron et al., 1991], Mount Pinatubo [Bluth et al., 1992a], and Mount Spurr [Bluth et al., 1992b]. In addition, the TOMS data archive (which dates back to 1979) has been used to estimate the contribution of explosive eruptions to the global SO_2 budget [Bluth et al., 1993].

Read et al. [1993] showed that MLS data, acquired from the Upper Atmosphere Research Satellite (UARS), could be used to recover altitude profiles of the SO_2 clouds produced by the Pinatubo eruption. The MLS procedure is sensitive to SO_2 concentrations as low as 3 ppb(v).

Realmuti et al. [1994] recently demonstrated that thermal IR image data could be used to map the SO_2 content of volcanic plumes. This technique was developed using TIMS data acquired at Mount Etna, Sicily on 26 July

1986, when the estimated column abundance of SO_2 within the plume ranged from 1 to 17 g m^{-2} and the overall flux was estimated at 78 kg/s. The TIMS-based estimation technique is based on the detection of a broad feature between 8 and 9.5 μm in the absorption spectrum of SO_2 . The maximum absorption is located at 8.5 μm , and falls between the first and second channels of TIMS. The estimation procedure is based on radiative transfer modeling, which is used to fit the radiance observed by TIMS as it views the ground through an intervening SO_2 plume. Based on the data collected at Mount Etna in 1986, the TIMS-based procedure has an estimation error of approximately 15%.

4.1. Applications to Mount Loa eruption plumes

The 1984 eruption of Mount Loa began on 25 March and ended on 14 April [Lockwood et al., 1985; Smithsonian Institution, 1989; Casadevall et al., 1984]. On the first day of the eruption, the plume reached an altitude of approximately 11 km. The plume did not reach the stratosphere, since the tropopause was at an altitude of 18 km. Between 27 March and 14 April 1984 the maximum altitude of the plume was less than 4.6 km. During this period the plume travelled westward at a rate of 800 km/d, reducing visibility at airports up to 5000 km away from Mount Loa.

The flux rates of SO_2 and CO_2 were determined with a series of airborne COSPEC and infrared analyzer surveys of the plume [Casadevall et al., 1984]. Between 2 April and 14 April the flux of SO_2 ranged between 2200 and 6600 $\times 10^3$ kg per day, while the flux of CO_2 ranged between 240 and 1400 $\times 10^3$ kg per day. Estimates of the SO_2 column abundance with TOMS indicated a maximum of approximately 2 g m^{-2} on 27 March. TOMS data were also used to estimate that the Mount Loa plume contained 130,000 $\times 10^3$ kg of SO_2 on 26 March and 190,000 $\times 10^3$ kg on 27 March.

SO_2 abundances in the 26 July 1986 Mount Etna plume were estimated to be as much as eight times higher [Realuto et al., 1994] than those reported for the 1984 Mount Loa plume, yet the Etna plume was not detected by TOMS. This lack of detection is probably due to narrow width (1-5 km) and low altitude (<5 km MSL) of the Etna plume relative to the Mount Loa plume. The coarse spatial resolution of TOMS (50 km at nadir) is a limiting factor on the size of plume that can be detected.

5. REMOTE SENSING OF TEMPERATURE

Multispectral remote sensing can be used for temperature determinations in volcanic regions [Francis and Rothery, 1987; Rothery, et al., 1988; Realuto, et al., 1992; Mougins-Mark, et al., 1994a; Flynn, et al., 1994]. While the techniques described here have not yet been used on Mount Loa, their use in the future seems likely. Because of the wide range of temperatures encountered, it is

desirable to acquire multispectral data from the visible and the shortwave infrared as well as the thermal infrared. While one commonly thinks of using the thermal infrared to measure temperature, in volcanic regions the radiation from very hot sources will saturate the majority of thermal IR sensors. Planck's Law indicates that the intensity of emitted radiation increases as a function of temperature, but also that the wavelength of the maximum emission shifts to progressively shorter wavelengths as the temperature increases. Figure 12, after Francis and Rothery [1987] shows a plot of radiance as a function of wavelength for a variety of different temperatures. The plot also includes the location and saturation level of the Landsat Thematic Mapper channels. When measuring very hot volcanic targets, one needs to select that wavelength region where the emitted radiation dominates over reflected radiation, but at the same time does not saturate the sensor. Rothery et al. [1988] and Oppenheimer et al. [1993] have also shown how using multiple wavelengths allows for the derivation of more than one temperature within a pixel — often the case where there is a small very hot area within a pixel while the majority of the pixel is near ambient temperature.

Ground-based spectroradiometric measurements, a study using the Advanced Very High Resolution Radiometer (AVHRR) and Landsat Thematic Mapper (TM) data, and work done using the NS001 and TIMS aircraft multispectral thermal data, have illustrated some of the applications of multispectral measurements to temperature observations of volcanic features on Kilauea, Hawaii, though not over Mauna Loa.

Using a spectroradiometer in the 0.4-2.5 μ m region, Flynn and Mouginiis-Mark [1992] and Flynn et al. [1993] made nighttime observations of active flows, and observations of the active Kupaianaha lava lake; both areas were on the East Rift Zone of Kilauea. They found that the crust of a newly emplaced lava flow cooled by about 350° in less than an hour. Their observations both are in agreement with, and help constrain theoretical models of flow emplacement. Over the Kupaianaha lava lake, they found that the temporal variability of the thermal output occurred on time scales of seconds to minutes, implying that satellite-based observations would, at best, provide only a snapshot of a rapidly changing phenomenon.

In a study examining the effects of viewing geometry on detection of thermal features in AVHRR weather satellite compared with Landsat Thematic Mapper, Mouginiis-Mark et al. [1994a] found that with nadir-looking, 1 km spatial resolution data, overturning lava lakes, surface flows, and lava tubes with skylights could be detected thermally. However, in off-nadir looking data, where the pixel size is as large as 14 km, some of the smaller of these phenomena could not be separated from solar heated, older lava flows. Using TM data, with 30 m spatial resolution, all of the phenomena could be detected thermally.

Realmutto et al. [1992] used TIMS thermal data acquired from the NASA C-130 to map the temperature distribution related to underground transport and storage of lava in the Kupaianaha flow field, Kilauea. Active lava

tubes were clearly mapped. The authors' temperature maps also defined the boundaries of hydrothermal plumes which resulted from entry of lava into the ocean. The multispectral data also allowed determination of emissivity variations attributed to acid-induced leaching near fumaroles (described earlier).

6. RADAR REMOTE SENSING OF MAUNALOA

6.1. Data coverage

In a comparable manner to visible and infrared imaging of the Earth's surface, radar systems provide the capability to observe the ground at several different wavelengths, polarizations, and viewing geometries. An attribute of all radar systems is that they can image the surface irrespective of cloud cover or time of day, thus complete coverage of the target can be obtained. The most important parameter in any radar investigation is the wavelength, which is typically either 3 cm (X-band), 5.6 cm (C-band), 24 cm (L-band) and 68 cm (P-band). Other parameters that can be varied are the polarization (horizontally-transmit and receive is denoted as "HH"; horizontally-transmit and vertically receive as "HV"; and vertically transmit and receive as "VV"), and the angle (called the "incidence angle") at which the radar energy hits the surface (typically in the range 20-60° from the nadir). Because radars provide their own illumination source, it is also possible to control the "look direction" of the instrument, so that structural features in a preferred orientation can be enhanced. The specific characteristics of the different radar systems that have been used to study Mauna Loa are summarized in Table 2.

Although Space Shuttle radar (SIR-B) data were collected over Kilauea volcano in October 1984 [Gaddis, et al., 1989, 1990], no radar data were collected over Mauna Loa until August 1990, when the NASA/JPL aircraft radar (AIRSAR) imaged extensive areas of the Big Island (Figure 13). More recently, a single image of the eastern half of the volcano was obtained in June 1993 by the spaceborne Japanese JERS-1 radar. The aircraft radar collected data over Hawaii in September 1993, [his time to perform topographic mapping of the southwestern flank of the volcano using the TOPSAR radar system [Zebker, et al., 1992]. TOPSAR can produce digital elevation models (DEMs) of landscapes at a spatial resolution of 10 m/pixel with a vertical accuracy of 2-5 m depending on the roughness of the terrain. These TOPSAR data for Mauna Loa have not yet been processed, but it is expected that the data will be of value for the measurement of lava flow thicknesses. TOPSAR data were collected across the 1950 lava flows in the hope that thickness variations associated with the local slope could be measured; good observations of the volumetric flow rate of these flows [Finch and Macdonald, 1950; Macdonald and Finch, 1950] should enable numerical models for the longitudinal variation in lava flow rheology [e. g., Fink and Zimbelman, 1989] to be tested.

The two flights of the Space Shuttle SIR-C/X-SAR

[Evans et al., 1993] radar also produced almost complete coverage of Mauna Loa and Kilauea volcanoes (Figure 13). The first SIR-C/X-SAR flight (in April 1994) was primarily devoted to using Kilauea as a calibration target for subsequent comparison with data obtained for other basaltic shield volcanoes around the world [Mouginis-Mark, 1994 b]. Nevertheless, most of the eastern side of Mauna Loa was also imaged (Data Take 52.1 at 52.30). Data were collected at three wavelengths (X-, C-, and L-band), various polarizations (HH, HV, and VV), multiple incidence angles (18-59°) on both ascending and, in one instance, a descending orbit. In most cases, only the eastern lower flank of Mauna Loa was imaged during these studies of Kilauea, except on the descending orbit when data for all 01° the northern half of Mauna Loa were obtained (Figure 13). During the second SIR-C/X-SAR mission (in October 1994), almost all of the western half of Mauna Loa was covered in a single data take (Data Take 36.10) at 32.1° incidence angle, complementing the April 1994 coverage of the eastern side of the volcano. Additional data for Mauna Loa were also obtained during the last four days of the mission when exact-repeat orbits were selected for radar interferometry experiments. Data were obtained at high resolution (12.5 m/pixel) over the 1989, 1942, and 1984 lava flows between the 1300-2000 m elevation levels. These data, which were obtained at C- and L-band VV-polarization) will be processed to produce a high resolution DEM as part of a broader investigation to study day-to-day variations in the distribution and thickness of the lava flow field of Kilauea.

6.2. Examples of radar observations

To date, the radar data for Mauna Loa have been largely ignored in favor of the comparable information for Kilauea volcano, due to the easier field logistics for data validation and the strong interest in the ongoing eruption at the Puu Oo vent for topographic change studies. For Kilauea, the primary use of the aircraft data has been the quantitative analysis of the molar backscatter properties of the individual lava flows [Campbell and Campbell, 1992], and their subsequent comparison to lava flows on Venus. Almost no investigations of the TOPSAR or SIR-C/X-SAR data for Hawaii have yet been published, but comparable analyses of other volcanoes [e. g., Mouginis-Mark and Garbeil, 1993; Mouginis-Mark, 1994b] suggest some of the studies that can be accomplished with the available data. In general, these studies focus on lithologic mapping, analyses of the structure of the volcano, the search for buried lava flows beneath ash deposits, and topographic mapping. All but the last of these applications can be demonstrated with Mauna Loa data collected in August 1990 by the AIRSAR system, and will now be briefly reviewed.

The use of multi-wavelength radar data to study differences in the surface roughness of lava flows has been well known for more than a decade. Using AIRSAR data, Campbell and Campbell (1992) showed that aa and pahoehoe-

hoe lava flows have different radar backscatter characteristics at L-band (24 cm). In the case of the summit of Mauna Loa (Figure 14), the multiwavelength radar enables different flow units to be identified, as well as subtle details of the structure of Mokuaweoweo caldera. Few of these phenomena have not been recognized from detailed field mapping [Macdonald, 1971; Lockwood et al., 1987]. The radar data show many flow contacts within the Mokuaweoweo overflow units more clearly than does conventional air photography, but the significance of some of these contacts has not yet been established. The difference in the radar and optical properties of the lava flows around Mokuaweoweo caldera can be seen from a comparison of the AIRSAR data and the SPOT satellite panchromatic (10 m/pixel) data presented in Figure 15.

Details of the structure of a volcano can often be enhanced using radar data; the careful selection of radar incidence angle and viewing direction can reveal subtle topographic features that may be difficult to identify due to the vegetation cover. Such an example is shown in Figure 16, which is part of the Ninole I [ills on the southeastern flank of Mauna Loa. This area, which is part of the Kau Forest Reserve, has proven to be difficult to map on the ground due to the dense vegetation [e.g., Lipman and Swenson, 1984; Lockwood, et al., 1988] and yet offers an insight into the earlier eruptive activity of the volcano. In particular, the P-band (68 cm) wavelength cross-polarized (XV) radar data provide some capabilities to image surface flows irrespective of the vegetation cover, and to infer subtle topographic features (arrowed in Figure 16) by virtue of tonal variations in the vegetation canopy. This break in slope is also evident on the JERS-2 and SIR-C radar images of the eastern flank of Mauna Loa, and so this appears to be a real feature. Parts of the Kahuku flow can be delineated in the radar image, although the Pohina flow is indistinguishable from the high background radar backscatter from the forests.

The ability of radar to penetrate dry, unconsolidated materials was first demonstrated through analysis of Space Shuttle (SIR-A) radar data for the Eastern Sahara [McCauley, et al., 1982], where buried drainage channels were identified beneath the desert sand. In the case of Mauna Loa, the South Point area at the distal end of the Southwest Rift Zone provides a similar opportunity for radar penetration studies, since there is 2-8 m of the Pahala ash in this area [Sterns and Macdonald, 1946, p. 73]. Particularly in the case of the longest radar wavelength (P-band, 68 cm), the possibility of delineating the edges of lava flows beneath the ash is high. Figure 17 shows one of the AIRSAR images of this area. A comparison between these radar data, air photographs and field observations shows that in addition to distinguishing individual lobes on the Puu Poo Pueo Flow mapped by J. Lockwood [pers. comm., 1995] the radar can detect braided flow boundaries that are reminiscent of lava channels can also be seen beneath the veneer of soil and wind-blown ash (e.g., pts. "D" and "E" in Figure 17). Other morphological features are also easily seen in the radar data, including wind streaks and dunes.

7. FUTURE REMOTE SENSING OF MAUNA LOA

Additional orbital radars will be used to study Hawaii. The European Space Agency (ESA) has been operating the ERS-1 radar since 1991, and [his has been used to study many of the volcanoes in Alaska and the Aleutians [Rowland, et al., 1994]. However, the ERS-1 spacecraft and its successor ERS-2, cannot currently be used to study any part of Hawaii due to the fact that the spacecraft do not carry onboard tape recorders. This requires that data are transmitted in real-time to ground stations that are in line of sight of the spacecraft. In order to collect ERS-2 and JERS-1 radar data, the University of Hawaii at Manoa (on the island of Oahu) is building a ground station specifically to study Mauna Loa and Kilauea using data from these satellites. It is expected that the Hawaii ground station will be operational by June 1995.

The ground reception capability for radar data of Hawaii creates the opportunity for extensive topographic and geodetic investigations of Hawaiian volcanoes. Using a technique called radar interferometry, which coherently compares the phase information contained within two radar images of the same scene, the value of the ERS-1 radar data in the analysis of ground movements associated with earthquakes was demonstrated for the 1992 Landers Earthquake in California [Massonnet, et al., 1993, 1994; Zebker, et al., 1994]. These radar observations enable ground movement at a fraction of a radar wavelength (typically ~ 3 mm in line-of-sight movement) to be identified over the entire image for dry targets in arid environments. Provided that the phase data from the radar can be correlated (the moist atmosphere in Hawaii may prove to be a problem at low elevations), such observations are predicted to be of great value for the study of ground deformation prior to a new eruption, or for the mapping of the planimetric shape of new lava flows [Mouginis-Mark, 1994c]. Current plans are for ERS-1 and ERS-2 to be flown in tandem so that exact-repeat coverage will be obtained once during a 24 hour interval sometime within a 35 day observation period. Following the expected demise of ERS-1 in late 1995, exact-repeat coverage will only be achieved from successive orbits of the ERS-2 spacecraft, which will have a 35-day repeat interval. JERS-1 radar data will also be collected every 24 days. Thus it should be possible to generate a deformation map of Mauna Loa approximately once per month.

The Canadian RADARSAT spacecraft [Raney et al., 1991] will also image Hawaii, except in this instance the data will be recorded on board. Data from RADARSAT will be particularly useful for frequent large-area coverage of the Big Island, due to the variable swath width, multiple incidence angles, and variable spatial resolution capabilities of the sensor. However, because of the lack of good navigation of the spacecraft (the absence of onboard GPS equipment), it is unlikely that RADARSAT data will be useful for interferometry experiments because the baseline separation of the orbits will not be known to an adequate accuracy. RADARSAT is planned for launch in early

1996.

A major improvement to optical remote sensing from space will occur in 1998 with the launch of the NASA'S Earth Observing System AM-1 platform, which will include the Advanced Spaceborne Thermal Emission and Reflection Radiometer (ASTER) and the Moderate-Resolution Imaging Spectrometer (MODIS). ASTER is a 14-channel imaging instrument, with bands in the VNIR, SWIR and TIR (Table 3). The pixel size is 15, 30 or 90 m, respectively for the three wavelength regions, with a repeat cycle of 16 days or less, depending on latitude; the swath width is 60 km [Kahle, et al., 1991]. MODIS will provide images in 36 bands between 0.4 and 14.5 μm with a pixel size of 250 m and 1 km. The 1 km resolution images will be available every one or two days. MODIS will thus allow monitoring on a 1-2 day basis while ASTER can be used for detailed process studies.

ASTER'S VNIR bands are similar to the Landsat TM bands and the TMS bands in this wavelength region, allowing detection of changes in iron oxidation and vegetation development. The SWIR bands will improve the capability to detect and map the development of clay minerals, associated with soil development and weathering in more humid climates. The spectral resolution of the ASTER TIR system is very similar to TIRS; therefore, ASTER should allow scientists to map both the change in surface properties of lava flows, and to map the SO_2 eruption plumes from Mauna Loa.

The improvement in pixel size of the thermal bands compared to AVHRR (90 m vs 1 km) will allow mapping of lava flows, lava tubes, and lava ponds, instead of just detecting them. It will also be possible to determine temperatures for volcanic features whose hottest components are smaller than a full pixel (generally the case for the flows, tubes and ponds). These new capabilities will improve our ability to map Mauna Loa, as well as other volcanoes worldwide.

Acknowledgements. We would like to acknowledge the thoughtful advice of manuscript reviewers David Rothery and Ronald Greeley. This work was performed at the Jet Propulsion Laboratory, California Institute of Technology, under contract to the National Aeronautics and Space Administration.

REFERENCES

- Abrams, M., E. Abbott, and A. Kahle, Combined use of visible, reflected and thermal infrared images for mapping 1 Hawaiian lava flows, J. Geophys. Res., 96, 475-484, 1991.
- Berresheim, H., and W. Jaeschke, The contribution of volcanoes to the global atmospheric sulfur budget, J. Geophys. Res., 88, 3732-3740, 1983.
- Bluth, G. J. S., S. D. Doiron, C. J. Scott, C. C. Schnetzler, A. J. Kreuger, and L. S. Walter, Global tracking of the SO₂ clouds from the June 1992 Mount Pinatubo eruptions, Geophys. Res. Lett., 19, 151-154, 1992a.
- Bluth, G. J. S., C. J. Scott, M. Schoeberl, C. C. Schnetzler, A. J. Kreuger, and L. S. Walter, SO₂ cloud tracking from the June and August eruptions of Mount Spurr, Alaska, Trans. Amer. Geophys. Union, 74, 614, 1992b.
- Bluth, G. J. S., C. C. Schnetzler, A. J. Kreuger, and L. S. Walter, The contribution of explosive volcanism to global atmospheric sulfur dioxide concentrations, -, 1.66, 327-329, 1993.
- Brawer, S. A., and W. B. White, Raman spectroscopic investigation of the structure of silicate glasses, 1, the binary alkali silicates, J. Chem. Phys., 63, 2421 - 2432, 1975.
- Caltabiano, L., R. Romano, and G. Budetta, SO₂ flux measurements at Mount Etna (Sicily), J. Geophys. Res., 99, 12809-12819, 1994.
- Campbell, B. A., and D. B. Campbell, Analysis of volcanic surface morphology on Venus from comparison of Arecibo, Magellan, and terrestrial radar data, J. Geophys. Res., 97, 16293-16314, 1992.
- Casadevall, T. J., D. A. Johnston, D. M. Harris, W. I. Rose, L. L. Malinconico, R. E. Stoiber, P. J. Bornhorst, S. N. Williams, L. Woodruff, and J. M. Thompson, SO₂ emission rates at Mount St. Helens from March 29 through December 1980, in USGS Prof. Paper 1250, edited by P. Lipman and D. R. Mullineaux, pp. 193-200, 1981.
- Casadevall, T. J., A. J. Krueger, and B. Stokes, The volcanic plume from the 1984 eruption of Mauna Loa, Hawaii, Trans. Amer. Geophys. Union, 65, 1133, 1984.
- Chartier, T. A., W. I. Rose, and J. B. Stokes, Detailed record of SO₂ emissions from Puu Oo between episodes 33 and 34 of the 1983-1986 ERX eruption, Kilauea, Hawaii, Bull. Volcanol., 50, 215-228, 1988.
- Crisp, J., A. Kahle, and E. Abbott, Thermal infrared spectral character of Hawaiian basaltic glasses, J. Geophys. Res., 95, 21657-21669, 1990.
- Curtiss, B., J. B. Adams, and M. S. Ghiorso, Origin development and chemistry of silica-alumina rock coatings from the semiarid regions of the island of Hawaii, Geochim. et Cosmochim. Acta, 49, 49-56, 1985.
- Doiron, S. D., G. J. S. Bluth, C. C. Schnetzler, A. J.

- Krueger, and L. S. Walter, Transport of Cerro Hudson SO_2 *CIOWIS*, Trans. Amer. Geophys. Union **72**, 489-498, 1991.
- Dowty, E., Vibrational interactions of tetrahedra in silicate glasses and crystals, 111, Calculations on simple sodium and lithium silicates, thorveitite and rankinite, Phys. Chem. Miner. **14**, 542-552, 1987.
- Evans D. L., C. Elachi, E. R. Stofan, B. Holt, J. B. Way, M. Kobrick, H. Ottl, P. Pampaloni, M. Vogt, S. Wall, J. van Zyl, and M. Schier, The Shuttle Imaging Radar-C and X-SAR mission, Eos, **74**, pp. 145, 157, 158, 1993.
- Farr, T., and J. Adams, Rock coatings in Hawaii, Geo. Soc. Amer. Bull. **95**, 1077-1083, 1984.
- Finch, R. Y., and G. A. Macdonald, The June 1950 eruption of Mauna Loa, Part 1, Volcano Letter, **508**, 12 pp., 1950.
- Fink, J., and J. Zimbelman, Longitudinal variations in theological properties of lavas: Puu 00 basalt flows, Kilauea volcano, Hawaii, in Lava Flows and Domes, IAVCEI Proc. Vole. vol. 2, edited by J. Fink, pp. 15-173, Springer-Verlag, New York, 1989.
- Flynn, L., and P. Mouginiis-Mark, Cooling rate of an active lava flow from nighttime spectroradiometer measurements, Geophys. Res. Lett., **19**, 1783-1786, 1992.
- Flynn, L., P. Mouginiis-Mark, J. Gradie, and P. Lucey, Radiative temperature measurements at Kupianaha Lava Lake, Kilauea Volcano, Hawaii, J. Geophys. Res., **98**, 6461-6476, 1993.
- Flynn, L. P., P. J. Mouginiis-Mark, and K. A. Horton, Distribution of thermal areas on an active lava flow field: Landsat observations of Kilauea, Hawaii, July 1991, Bull. Vole., **56**, 284-296, 1994.
- Francis, P. W., and D. A. Rothery, Using the Landsat Thematic Mapper to detect and monitor active volcanoes: An example from Lascar volcano, northern Chile, Geology, **15**, 614-617, 1987.
- Gaddis, L. R., P. J. Mouginiis-Mark, R. B. Singer, and V. H. Kaupp, Geologic analyses of Shuttle Imaging Radar (SIR-B) data of Kilauea Volcano, Hawaii, Geol. Soc. Amer. Bull., **ml**, 317-332, 1989.
- Gaddis, L. R., P. J. Mouginiis-Mark, and J. Hayashi, Lava flow surface textures: SIR-B radar image texture, field observations, and terrain measurements, Photogram. Eng. Rem. Sen., **56**, 211-224, 1990.
- Gillespie, A. R., Digital techniques of image enhancement, in Remote Sensing in Geology, edited by B. Siegal and A. Gillespie, pp. 139-226, John Wiley, New York, 1980.
- Gillespie, A. R., A. B. Kahle, and R. E. Walker, Color enhancement of 1' highly correlated images, 1, Decorrelation and 1 ISI contrast stretches, Remote Sens. Environ., **20**, 209-235, 1986.
- Hamilton, P. M., R. H. Valey, and M. M. Millán, Remote sensing of sulfur dioxide, Atmos. Environ., **12**, 127-133, 1978.

- Hoff, R. M., and M. M. Millán, Remote SO₂ mass flux measurements using COSPEC, J. Air Pollut. Control Assoc., **31**, 381-384, 1981.
- Holcomb, R. T., Eruptive history and long-term behavior of Kilauea volcano, in Volcanism in Hawaii, Volume 1, U.S. Geol. Surv. Prof. Pap. 1350, edited by R. W. Decker, P. H. Wright, and P. H. Stauffer, pp. 261-350, 1987.
- Hunt, G., Spectral signatures of particulate minerals in the visible and near infrared, Geophys., **42**, 501-513, 1977.
- Kahle, A. B., A. R. Gillespie, E. A. Abbott, M. J. Abrams, R. E. Walker, G. Hoover, and J. P. Lockwood, Relative dating of Hawaiian lava flows using multispectral thermal infrared images: A new tool for geologic mapping of young volcanic terranes, J. Geophys. Res., **93**, 15239-15251, 1988.
- Kahle, A. B., F. D. Palluconi, S. J. Hook, V. J. Realmuto, and G. Bothwell, The Advanced Spaceborne Thermal Emission and Reflectance Radiometer (ASTER), Int'l J. Imaging Sys. Tech., **3**, 144-156, 1991.
- Krueger, A. J., Sighting of El Chichón sulfur dioxide clouds with the Nimbus 7 Total Ozone Mapping Spectrometer, Science, **220**, 1377-1379, 1983.
- Krueger, A. J., Detection of volcanic eruptions from space by their sulfur dioxide clouds, AIAA-85-0100, AIAA 23rd Aerospace Science Meeting, Reno, Nevada, 1985.
- Krueger, A. J., L. S. Walter, C. C. Schnetzler, and S. D. Doiron, TOMS measurement of the sulfur dioxide emitted during the 1985 Nevado del Ruiz eruptions, J. Volcanol. Geotherm. Res., **41**, 7-15, 1990.
- Lipman, P. W., and A. Swenson, Generalized geologic map of the Southwest Rift Zone of Mauna Loa, Hawaii, U.S. Geological Survey Miscellaneous Investigation Series Map 1-1323, 1984.
- Lockwood, J. P., N. Banks, T. English, L. Greenland, D. Jackson, D. Johnson, R. Koyanagi, K. McGee, A. Okamura, and J. Rhodes, The 1984 eruption of Mauna Loa volcano, Hawaii, EOS Trans. Amer. Geophys. Union, **66**, 169-171, 1985.
- Lockwood, J. P., J. J. Dvorak, T. T. English, R. Y. Koyanagi, A. T. Okamura, M. L. Summers, and W. R. Tanigawa, Mauna Loa 1074---1984: A decade of intrusive and extrusive activity, in Volcanism in Hawaii, U.S. Geological Survey Prof. Paper 1350, pp. 537-570, 1987.
- Lockwood, J., and P. Lipman, Holocene eruptive history of Mauna Loa, in Volcanism in Hawaii, Volume 1, U.S. Geol. Surv. Prof. Paper 1350, edited by R. Decker, and P. Stauffer, 1987.
- Lockwood, J. P., P. W. Lipman, L. D. Petersen, and F. R. Warshauer, Generalized ages of surface lava flows of Mauna Loa volcano, Hawaii, U.S. Geol. Surv. Misc. Inv. Map, 1-1908, 1988.
- Macdonald, G. A., Geologic map of the Mauna Loa Quadrangle, Hawaii, U.S. Geological Survey Geologic Map, Mauna Loa Quadrangle, Hawaii, GQ-897, 1971.

- Macdonald, G., and R. Y. Finch, The June 1950 eruption of Mauna Loa, Part 2, Volcano Letters, 509, 1-6, 1950.
- Malinconico, L. L., Fluctuations in SO₂ emission during recent eruptions 0111[[1: Nature, 278, 43-45, 1979.
- Malinconico, L. L., On the variation of SO₂ emissions from volcanoes, J. Volcanol. Geotherm. Res., 33, 231-237, 1987.
- Massonnet, D., K. Feigl, M. Rossi, and F. Adragna, Radar interferometric mapping of deformation in the year after the Landers earthquake, Nature, 369, 227-230, 1994.
- Massonnet, D., M. Rossi, C. Carmona, F. Adragna, G. Peltzer, K. Feigl, and P. Rabaute, The displacement field of the Landers earthquake mapped by radar interferometry, Nature, 364, 13-142, 1993.
- McCauley, J. P., G. G. Schaber, C. S. Breed, M. J. Grolier, C. V. Haynes, B. Issawi, C. Elachi, and R. Blore, Subsurface valleys and geoarcheology of the eastern Sahara revealed by Shuttle radar, Science, 218, 1004-1020, 1982.
- Moffat, A. J., and M. M. Millán, The applications of optical correlation techniques [0 the remote sensing of SO₂ plumes using sky light, Atmos. Environ., 5, 677-690, 1971.
- Mouginis-Mark, P. J., and H. Garbeil, Digital topography of volcanoes from radar interferometry: An example from Mt. Vesuvius, Italy, Bull. Volcan., 55, 566-570, 1993.
- Mouginis-Mark, P., H. Garbeil, and P. Flament, Effects of viewing geometry on AVHRR observations of volcanic thermal anomalies, Rem. Sens. Environ., 48, 51-60, 1994a.
- Mouginis-Mark, P. J., Preliminary observations of volcanoes with the SIR-C/X-SAR radar. Submitted to IEEE Trans. Geosci. Rem. Sen., 1994b.
- Mouginis-Mark, P. J., Mitigating volcanic hazards through radar interferometry, Geotimes, July, 11-13, 1994c.
- Oppenheimer, C., P. Francis, D. Rothery, R. Carlton, and L. Glaze, Infrared image analysis of volcanic thermal features: Lascar volcano, Chile, 1984-1992, J. Geophys. Res., 98, 4269-4286, 1993.
- Palluconi, F. D., and G. R. Meeks, Thermal infrared multispectral scanner (T1 MS): An investigator's guide to T1MS data, JPL Publ., 85-32, 1985.
- Raney, R. K., A. P. Luscombe, E. J. Langham, and S. Ahmed, RADARS AT, Proc. IEEE, 79, 839-849, 1991.
- Read, W. (3., L. Froidevaux, and J. W. Waters, Microwave Limb Sounder (MLS) measurements of SO₂ from Mt. Pinatubo volcano, Geophys. Res. Lett., 20, 1209-1302, 1993.
- Realmuto, V. J., M. J. Abrams, M. F. Buongiorno, and D. C. Pieri, The use of multispectral thermal infrared image data to estimate the sulfur dioxide flux from volcanoes: A case study from Mount Etna, Sicily, July 29, 1986, J. Geophys. Res., 99, 481-488, 1994.
- Realmuto, V. J., K. Hon, A. B. Kahle, E. A. Abbott, and D. C. Pieri, Multispectral thermal infrared mapping of

- the 1 October 1988 Kupaianaha flow field, Kilauea volcano, Hawaii, Bull. Volc., 55, 33-44, 1992.
- Rotbery, D. A., P. W. Francis, and C. A. Wood, Volcanic monitoring using short wavelength infrared data from satellites, J. Geophys. Res., 93, 7993-8008, 1988.
- Rowland, S. K., G. A. Smith, and P. J. Mouginiis-Mark, Preliminary ERS-1 observations of Alaskan and Aleutian volcanoes, Remote Sens. Environ., 48, 358-369, 1994.
- Simon, I., and H. O. McMahon, Study of some binary silicate glasses by means of reflection in infrared, J. Am. Ceram. Soc., 36, 160-164, 1953.
- Smithsonian Institute, Global Volcanism 1975-1985, Prentice Hall, New Jersey, and American Geophysical Union, Washington, DC, 657 pp., 1989.
- Stearns, I. T., and G. A. Macdonald, Geology and groundwater resources of the Island of Hawaii, Hawaii Divn. Hydrography. Bull., 9, 363 pp., 1946.
- Stoiber, R. E., L. L. Malinconico, and S. N. Williams, Use of the correlation spectrometer at volcanoes, in Forecasting Volcanic Events, edited by I. I. Tazieff and J. C. Sabroux, Elsevier, pp. 425-444, 1983.
- Stoiber, R. E., S. N. Williams, and B. Huebert, Annual contribution of sulfur dioxide to the atmosphere by volcanoes, J. Volcanol. Geotherm. Res., 33, 1-8, 1987.
- Zebker, H. A., S. N. Madsen, J. Martin, K. B. Wheeler, 'P', Miller, Y. Lou, G. Alberti, S. Vetrella, and A. Cucci, 1992, The TOPSAR interferometric radar topographic mapping instrument, IEEE Trans. Geosci. Rem. Sens., 30, 933-940, 1992.
- Zebker, H. A., P. Rosen, R. M. Goldstein, A. Gabriel, and C. L. Werner, On the derivation of coseismic displacement fields using differential radar interferometry: The Landers earthquake, J. Geophys. Res., 99, 14517-14534, 1994.

TABLE 1. Band Passes of Scanners

NS001		TIMS	
CHANNEL	WAVELENGTH, μm	CHANNEL	WAVELENGTH, μm
1	0.45—0.52	1	8.2—8.6
2	0.52—0.60	2	8.6—9.0
3	0.63—0.69	3	9.0—9.5
4	0.76—0.90	4	9.6—10.2
5	1.0—1.30	5	10.2—11.2
6	1.55—1.75	6	11.2—11.7
7	2.08—2.36		
8	10.4—12.5		

TABLE 2. Characteristics of Radar Systems That Have Imaged Mauna Loa

Sensor	Wavelength ^a	Pixel size	Angle	Polarization
AIRSAR	C, L, P	12.5 m/pixel	20-600	HH, HV, VH, VV
TOPSAR	L, P	12.5 m/pixel	20-600	HH, HV, VH, VV
	C	12.5 m/pixel	20-600	VV
JERS-1	L	18 m/pixel	35°	HH
SIR-C ^b	X, C, L	25 m/pixel	56° and 60°	X-VV, C-VV, L-HH
ERS-2 ^c	C	25 m/pixel	23°	VV
RADARSAT3	C	25, 50, 100 m/p	20-50°	HH

^aRadar wavelengths are as follows: X-band is 3 cm, C-band is 5.6 cm, L-band is 24 cm, and P-band is 68 cm.

^bSIR-C/X-SAR operated in many different wavelength/polarization modes [Evans et al., 1993]. Only those that were used to image Hawaii are given here.

^cFuture radar system if value for Mauna Loa studies.

TABLE 3. ASTER Channels and Wavelength (μm)

VNIR		SWIR		TIR	
1	0.52-0.60	4	1.600-1.700	10	8.125-8.475
2	0.63-0.69	5	2.145-2.185	11	8.475-8.825
3	0.76-0.86	6	2.185-2.225	12	8.925-9.275
		7	2.235-2.285	13	10.25-10.95
		8	2.295-2.365	14	10.95-11.65
		9	2.360-2.430		

Figure Captions — 15.5 cm wide

Figure 1. Index map of the island of Hawaii showing location of images discussed in this paper.

Figure 2. Laboratory reflectance spectra of green vegetation and Mauna Loa aa and pahoehoe flows dating from 1935, 1899, 200-500 years BP, 500-1500 years BP, 1500-4000 years BP and 4000-9000 years BP. Reflectance values at $0.8 \mu\text{m}$ are indicated above each curve. Spectra have been offset vertically for clarity. Positions of NS001 channels are indicated above the graphs.

Figure 3. Laboratory spectrum of a cooled sample collected from an active Puu Oo flow in May, 1989. TIMS channel locations are shown on upper axis. The laboratory spectrometer measures reflectance, which is equal to $(1 - \text{emissivity})$ according to Kirchhoff's law.

Figure 4. Laboratory reflectance spectra of Mauna Loa lavas collected along the Hilo-Kona jeep trail (Figures 5 and 6). Letters A, B, and C refer to spectral features discussed in the text.

(a) aa

(b) Pahoehoe

Figure 5. Laboratory reflectance spectra of aa and pahoehoe of the same age (0.2- 0.5 ka) which have been normalized.

Figure 6. A decorrelation stretched TIMS image of part of the north flank of Mauna Loa. Bands 1, 3, and 5 are displayed in blue, green and red, respectively. Age and vegetation cover information are given in Figure 7.

Figure 7. Index map for Mauna Loa TIMS image (Plate 1) showing flow outlines and ages (dates for historical flows; radiocarbon age groups for prehistoric flows I = 0.2—0.5 ka; II = 0.5—1.5 ka; III = 1.5-4 ka; IV = 4-8 ka; V = >8 ka); "a" is aa; "p" is pahoehoe. Circles mark location for samples of Figure 3. Numbers in boxes give the vegetation cover measured in the field for selected flows [J. B. Adams, personal communication, 1988].

Figure 8. NS001 principal components image. Bands 1 through 7 were used for the analysis. The loadings for component 2, displayed in red, produced a difference between the IR and VIS bands; component 3, in green, was heavily loaded as the difference between bands 3 and 1; component 4, in blue, was heavily loaded as the difference between bands 4 and 7. The overlay shows interpreted flow contacts, with age labels as in Plate 1; p = pahoehoe; a = aa; Op = undifferentiable prehistoric pahoehoe; 43a = 1843aa; 35a = 1935aa.

Figure 9. TIMS decorrelation stretched image of the Mauna Loa test area. Bands, 1, 3, and 5 are displayed in blue, green, and red, respectively. The overlay shows interpreted flow contacts, with age labels as in Plate 1; p = pahoehoe; a = aa; units labeled "a" alone = undifferentiable aa; 35p = 1935p; 43p = 1843p.

Figure 10. Combined NS001 and TIMS data processed using a principal components transformation. NS001 bands 1 through 7, and TIMS bands 1 through 6 were used for the analysis. PC1, PCS, PC6 displayed in red, green and blue, respectively. The overlay shows interpreted flow contacts, with age labels as in Plate 1; p = pahoehoe; a = aa; 35a(p) = 1935a(p); 43a(p) = 1843a(p).

Figure 11. Geologic map of the Mauna Loa test site. Spectral sample sites are indicated by numbers 1-12; p = pahoehoe; a = aa; I = unit I (0.2--0.5 ka); 2 = unit II (0.5—1.5 ka); 3 = unit III (1.5-4 ka); 4 = unit IV (4—8 ka); 5 = unit V (>8 ka). Modified from J. Lockwood [unpublished data, 1988].

Figure 12. Wavelength dependence of thermal radiance, according to Planck's formula, for surfaces with a uniform emissivity 0.8, plotted for a range of temperatures. The boxes indicate the band passes and operational range of radiance for the visible and shortwavelength infrared Landsat Thematic Mapper (TM) sensors. Alter Francis and Rothery, 1987.

Figure 13. Maps showing the coverage of Mauna Loa with imaging radar systems. Areas in red show

places where data were collected in 1990 (left), 1993 (center) and 1994 (right). The AIRSAR data collected in 1990 were obtained with multiple parallel flight lines, so that there is some overlapping coverage at different incidence angles along the center of each of the three broad bands shown here. The large square in the 1993 map shows the location of the JER-1 data, and the smaller area on the southwestern tip of the island marks the location of the TOPSAR data. The map for the 1994 SIR-C data shows the coverage that was obtained during the two flights in April and October, 1994. SIR-1 Data Take 52.1 provides the coverage that extends from South Point to Falea, SIR-1 Data Take 122.2 the coverage from Kohala and Hualalai to Kilauea, and SIR-2 Data Take 36.1 the coverage of western Mauna Loa. Additional data were also collected by SIR-2 in October 1994 at higher spatial resolution (12.5 m/pixel) for subareas within this broader coverage.

Figure 14. AIRSAR aircraft radar image of Mokuaweoweo caldera, obtained August 6, 1990. The geometry of the caldera is distorted due to the oblique viewing geometry of the radar. This image is a combination of P-band HV displayed in red, L-band HV displayed in green, and C-band HV displayed in blue. The viewing direction is from the east, and the incidence angle varies from 35° in the near-range to 62° in the far-range. This combination of radar wavelengths and polarizations enhances the differences between the historical aa flows (in green) and the prehistoric pahoehoe flows (in purple). Other features can also be identified: (a) the 1975 and 1984 flows in South Pit; (b) the ash deposit associated with the 1949 cone; (c) individual flow lobes in the latest prehistoric flows [Macdonald, 1971]; (d) segments of the 1984 lava flows on the floor of North Pit; and (e) the 1940 cone. Also visible (arrowed) is the 1984 eruptive vent,

Figure 15. SPOT panchromatic image of Mokuaweoweo caldera, showing the area included in the AIRSAR image (Figure 14). Notice that at optical wavelengths the shelly, "leu[te]l[ite]-rich", pahoehoe flows appear darker than older, dense, "tube-fed" pahoehoe, and aa appears darker than pahoehoe of equivalent or younger ages. North is towards the top.

Figure 16. AIRSAR aircraft radar image of part of the Ninole I hills on the eastern flank of Mauna Loa, obtained August 4th, 1990. This image is a combination of P-band HV displayed in red, L-band HV displayed in green, and C-band HV displayed in blue. The viewing direction is from the west, and the incidence angle varies from 35° in the near-range to 62° in the far-range. The P-band data enables the 1950 Kahuku flow ("A") to be identified, but the prehistoric Pohina flow ("B") has radar backscatter characteristics that are comparable to the rain forest and so cannot be discriminated. Notice that no other flow margins can be identified in this scene, so that this radar data set cannot be used to extend existing geologic maps of the area. The radar does, however, clearly delineate the Makaalia ridge ("C"), and subtle breaks in slope (arrows point down slope). Two jeep tracks ("D") can also be seen. Image width is 12 km, the viewing direction is from the left.

Figure 17. AIRSAR aircraft radar image of the South Point area on the distal end of the Southwest Rift Zone of Mauna Loa, obtained August 4th, 1990. This image is a combination of P-band HV displayed in red, L-band HV displayed in green, and P-band VV displayed in blue. The viewing direction is from the northwest (top of image), and the incidence angle varies from 35° in the near-range to 60° in the far-range. At "A", several lobes of the 7.2 Ka Puu Poo Poo Flow (which is covered by 20-40 cm of ash) can be identified. The 1868 flow is at "B". By virtue of the look-direction, the sea cliff and Pali o Mamalu (black arrows) is clearly seen. Dunes are located at "C". The combination of two P-band polarizations is particularly good at showing the morphology of flows that lie beneath a surficial layer of the Pahala Ash, which is 2-8 m thick at this locality [Stearns and Macdonald, 1946] and is predominately dark green in this image. This penetration enables the structure of some near-surface prehistoric flows to be seen at "D" and "E". Interestingly, the barren 1868 flow ("B") has the same radar characteristics as flow "D", which is deeply covered in ash. No fieldwork to investigate these radar properties has, however, been done at this time. The light at South Point is at "F". The white arrows point to several of the numerous wind streaks that have formed in the loose surficial materials in response to the prevailing trade winds. Image width is 13 km.

Figure Captions — 8 cm wide

Figure 1. Index map of the island of Hawaii showing location of images discussed in this paper.

Figure 2. Laboratory reflectance spectra of green vegetation and Mauna Loa aa and pahoehoe flows dating from 1935, 1899, 200-500 years BP, 500-1500 years BP, 1500-4000 years BP and 4000-9000 years BP. Reflectance values at $0.8 \mu\text{m}$ are indicated above each curve. Spectra have been offset vertically for clarity. Positions of NS001 channels are indicated above the graphs.

Figure 3. Laboratory spectrum of a cooled sample collected from an active Puu Oo flow in May, 1989. TIMS channel locations are shown on upper axis. The laboratory spectrometer measures reflectance, which is equal to $(1 - \text{emissivity})$ according to Kirchhoff's law.

Figure 4. Laboratory reflectance spectra of Mauna Loa lavas collected along the Hilo-Kona jeep trail (Figures 5 and 6). Letters A, B, and C refer to spectral features discussed in the text.

- (a) aa
- (b) Pahoehoe

Figure 5. Laboratory reflectance spectra of aa and pahoehoe of the same age (0.2 — 0.5 ka) which have been normalized.

Figure 6. A decorrelation stretched TIMS image of part of the north flank of Mauna Loa. Bands 1, 3, and 5 are displayed in blue, green and red, respectively. Age and vegetation cover information are given in Figure 7.

Figure 7. Index map for Mauna Loa TIMS image (Plate 1) showing flow outlines and ages (dates for historical flows; radiocarbon age groups for prehistoric flows I = 0.2—0.5 ka; II = 0.5–1.5 ka; III = 1.5–4 ka; IV = 4–8 ka; V = >8 ka); "a" is aa; "p" is pahoehoe. Circles mark location for samples of Figure 3. Numbers in boxes give the vegetation cover measured in the field for selected flows [L. B. Adams, personal communication, 1988].

Figure 8. NS001 principal components image. Bands 1 through 7 were used for the analysis. The loadings for component 2, displayed in red, produced a difference between the IR and VIS bands; component 3, in green, was heavily loaded as the difference between bands 3 and 1; component 4, in blue, was heavily loaded as the difference between bands 4 and 7. The overlay shows interpreted flow contacts, with age labels as in Plate 1; p = pahoehoe; a = aa; Op = undifferentiable prehistoric pahoehoe; 43a = 1843aa; 35a = 1935aa.

Figure 9. TIMS decorrelation stretched image of the

Mauna Loa test area. Bands, 1, 3, and 5 are displayed in blue, green, and red, respectively. The overlay shows interpreted flow contacts, with age labels as in Plate 1: P = pahoe-hoe; a = aa; units labeled "a" alone = undifferentiated aa; 35p = 1935p; 43p = 1843p.

Figure 10. Combined NS001 and TIMS data processed using a principal components transformation. NS001 bands 1 through 7, and TIMS bands 1 through 6 were used for the analysis. PC 1, PC 5, PC 6 displayed in red, green and blue, respectively. The overlay shows interpreted flow contacts, with age labels as in Plate 1; p = pahoe-hoe; a = aa; 35a(p) = 1935a(p); 43a(p) = 1843a(p).

Figure 11. Geologic map of the Mauna Loa test site. Spectral sample sites are indicated by numbers I-12: p = pahoe-hoe; a = aa; 1 = unit I (0.2-0.5 ka); 2 = unit II (0.5-1.5 ka); 3 = unit III (1.5-4 ka); 4 = unit IV (4-8 ka); 5 = unit V (>8 ka). Modified from J. Lockwood [unpublished data, 1988].

Figure 12. Wavelength dependence of thermal radiance, according to Planck's formula, for surfaces with a uniform emissivity of 0.8, plotted for a range of temperatures. The boxes indicate the band passes and operational range of radiance for the visible and shortwavelength infrared Landsat Thematic Mapper (TM) sensors. After Francis and Rothery, 1987.

Figure 13. Maps showing the coverage of Mauna Loa with imaging radar systems. Areas in red show places where data were collected in 1990 (left), 1993 (center) and 1994 (right). The AIRSAR data collected in 1990 were obtained with multiple parallel flightlines, so that there is some overlapping coverage at different incidence angles along the center of each of the three broad bands shown here. The large square in the 1993 map shows the location of the JERS-1 data, and the smaller area on the southwestern tip of the island marks the location of the TOPSAR data. The map for the 1994 SIR-C data shows the coverage that was obtained during the two flights in April and October, 1994. SRL-1 Data Take 52.1 provides the coverage that extends from South Point to Hilo, SRL-1 Data Take 122.2 the coverage from Kohala and I Iualalai to Kilauea, and SRL-2 Data Take 36.1 the coverage of western Mauna Loa. Additional data were also collected by SRL-2 in October 1994 at higher spatial resolution (12.5 in/pixel) for sub-areas within this broader coverage.

Figure 14. AIRSAR aircraft radar image of Mokuawe-oweo caldera, obtained August 6, 1990. The geometry of the caldera is distorted due to the oblique viewing geometry of the radar. This image is a combination of P-band HV displayed in red, L-band HV displayed in green, and C-band HV displayed in blue. The viewing direction is from the east, and the incidence angle varies from 35° in the near-range to 62° in the far-range. This

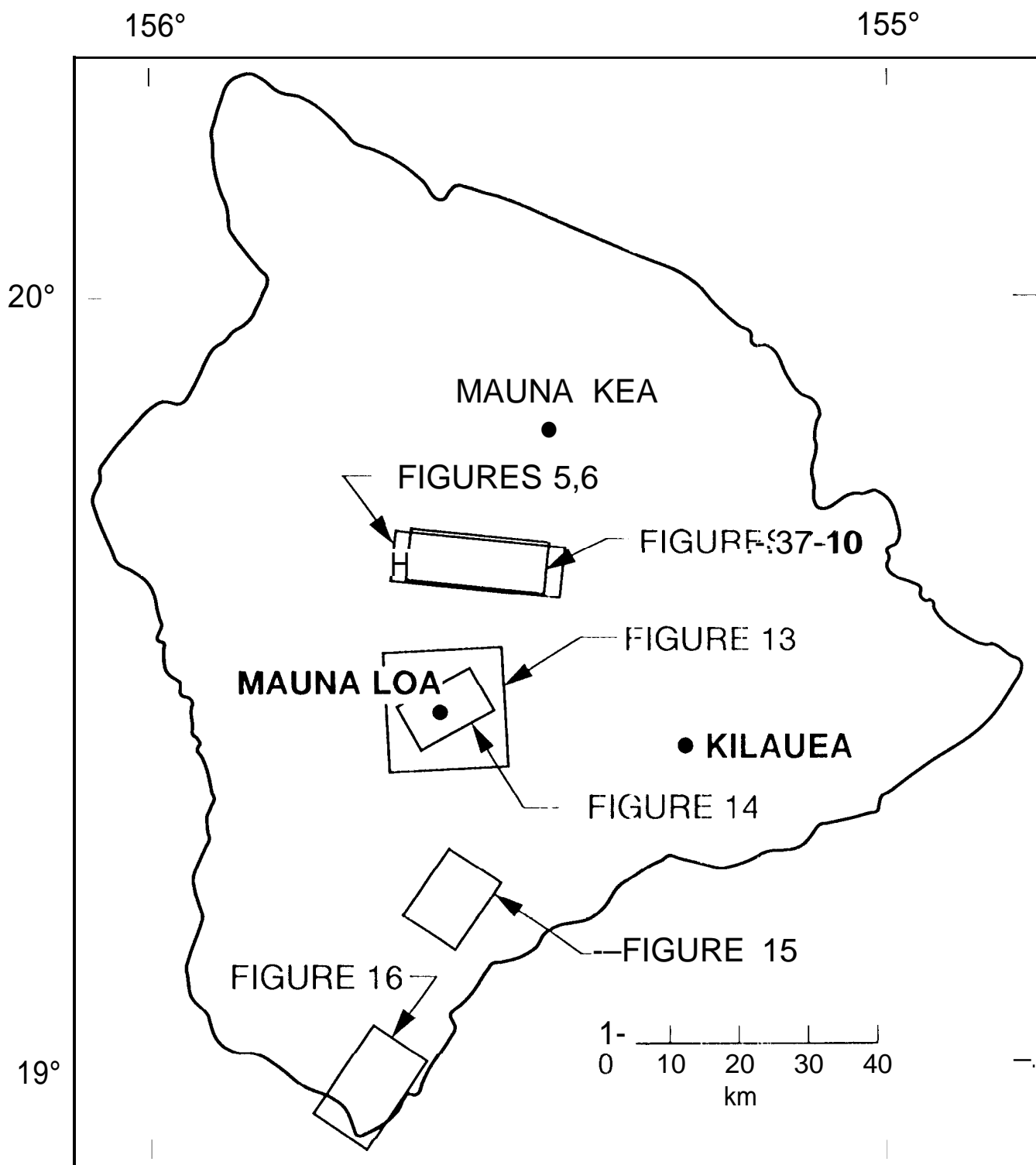
combination of radar wavelengths and polarizations enhances the differences between the historical aa flows (in green) and the prehistoric pahoehoe flows (in purple). Other features can also be identified: (a) the 1975 and 1984 flows in South Pit; (b) the ash deposit associated with the 1949 cone; (c) individual flow lobes in the latest prehistoric flows [Macdonald, 1971]; (d) segments of the 1984 lava flows on the floor of "North Pit"; and (e) the 1940 cone. Also visible (arrowed) is the 1984 eruptive vent.

Figure 15. SPOT panchromatic image of Mokuaweoweo caldera, showing the area included in the AIRSAR image (Figure 14). Notice that at optical wavelengths the shelly, "fountain-fed" pahoehoe flows appear darker than older, dense, "tube-fed" pahoehoe, and aa appears darker than pahoehoe of equivalent or younger ages. North is towards the top.

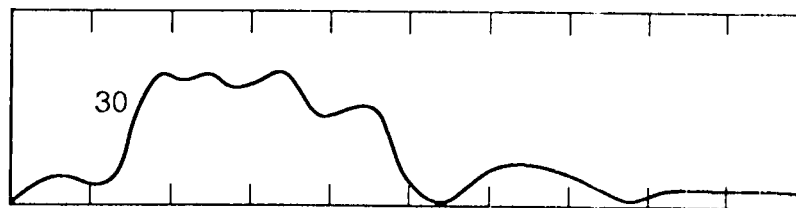
Figure 16. AIRSAR aircraft radar image of part of the Ninole Hills on the eastern flank of Mauna Loa, obtained August 4th, 1990. This image is a combination of P-band HV displayed in red, L-band HV displayed in green, and C-band HV displayed in blue. The viewing direction is from the west, and the incidence angle varies from 35° in the near-range to 62° in the far-range. The P-band data enables the 1950 Ka'ahu flow ("A") to be identified, but the prehistoric Pohina flow ("Er") has radar backscatter characteristics that are comparable to the rain forest and so cannot be discriminated. Notice that no other flow margins can be identified in this scene, so that this radar data set cannot be used to extend existing geologic maps of the area. The radar does, however, clearly delineate the Maka'ala ridge ("C"), and subtle breaks in slope (arrows point downslope). Two jeep tracks ("D") can also be seen. Image width is 12 km, the viewing direction is from the left.

Figure 17. AIRSAR aircraft radar image of the South Point area on the distal end of the Southwest Rift Zone of Mauna Loa, obtained August 4th, 1990. This image is a combination of P-band HV displayed in red, L-band HV displayed in green, and P-band VV displayed in blue. The viewing direction is from the northwest (top of image), and the incidence angle varies from 35° in the near-range to 60° in the far-range. At "A", several lobes of the 7.2 Ka Puu Poo Poo Flow (which is covered by 20-40 cm of ash) can be identified. The 1868 flow is at "B". By virtue of the look-direction, the sea cliff and Pali o Manalu (black arrows) is clearly seen. Dunes are located at "C". The combination of two P-band polarizations is particularly good at showing the morphology of flows that lie beneath a surficial layer of the Pahala Ash, which is 2-8 m thick at this locality [Stearns and Macdonald, 1946] and is predominately dark green in this image. This penetration enables the structure of some near-surface prehistoric flows to be seen at "D" and "E". Interestingly, the barren 1868

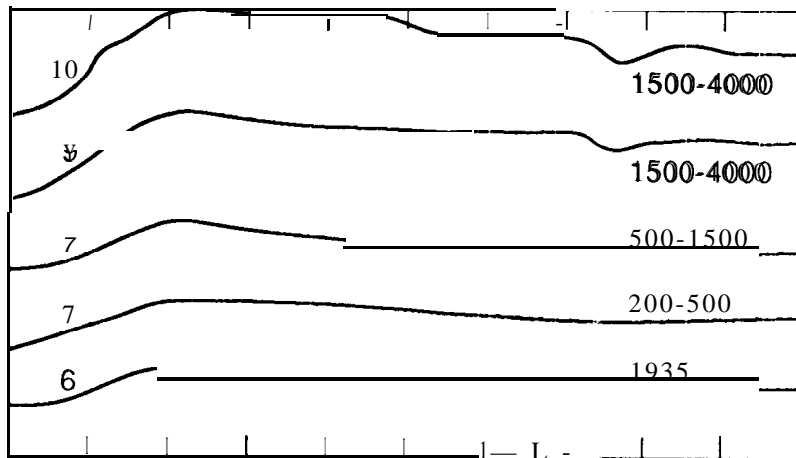
flow ("B") has the same radar characteristics as flow "D", which is deeply covered in ash. No field work to investigate these radar properties has, however, been done at this time. The light at South Point is at "F". The white arrows point to several of the numerous wind streaks that have formed in the loose surficial materials in response to the prevailing trade winds. Image width is 13 km.



1 2 3 4 L - J 5 6 7 NS001 BANDS

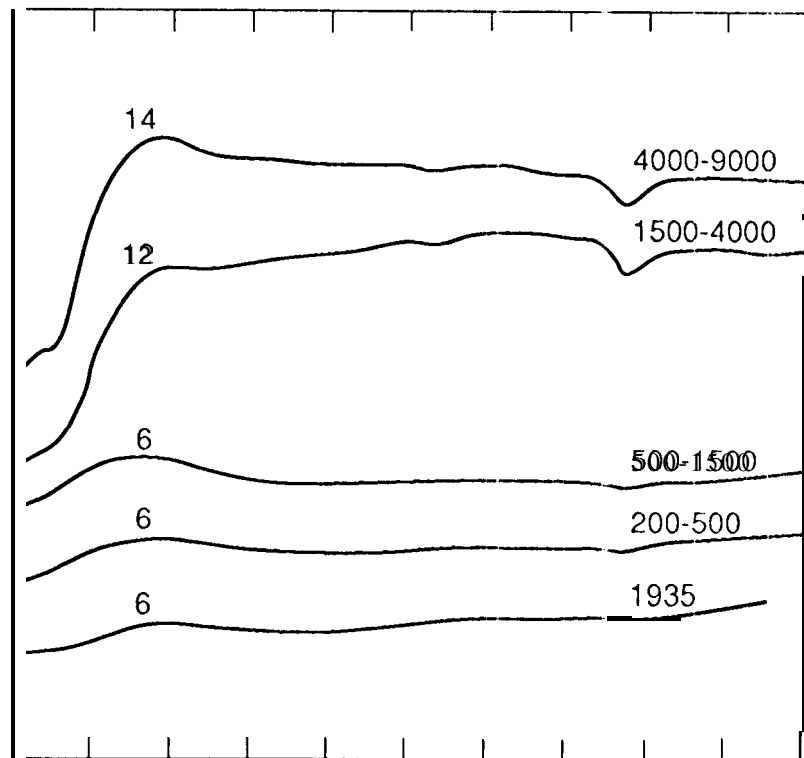


VEGETATION



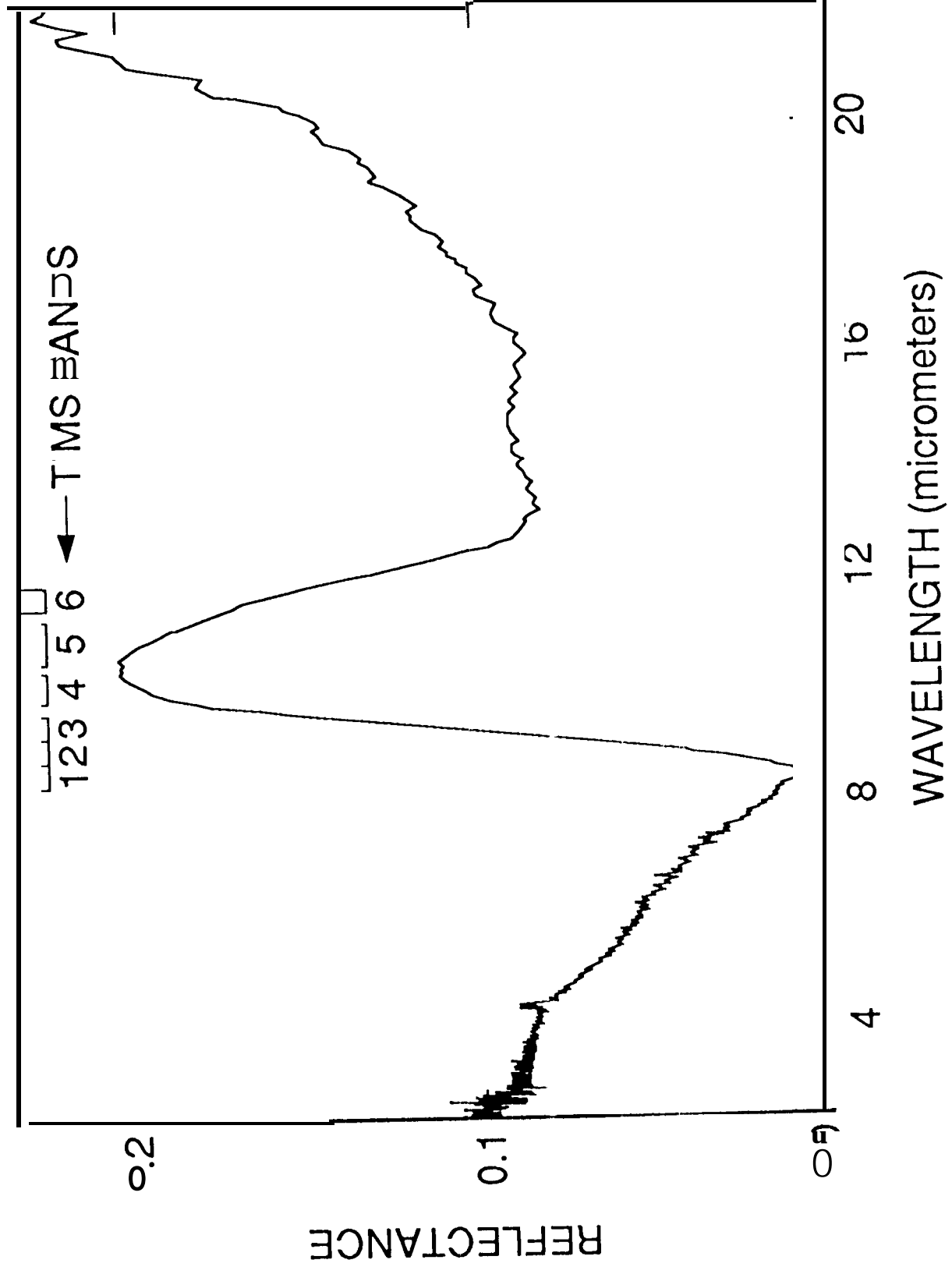
A A

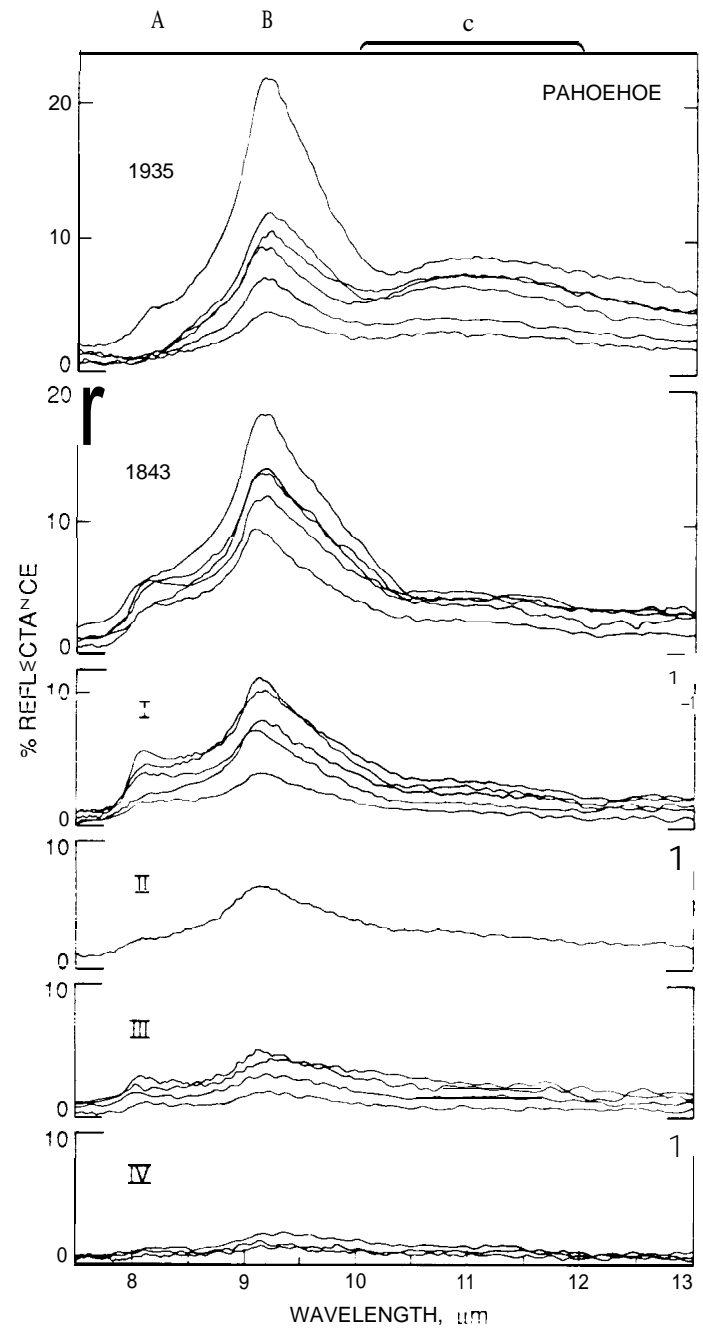
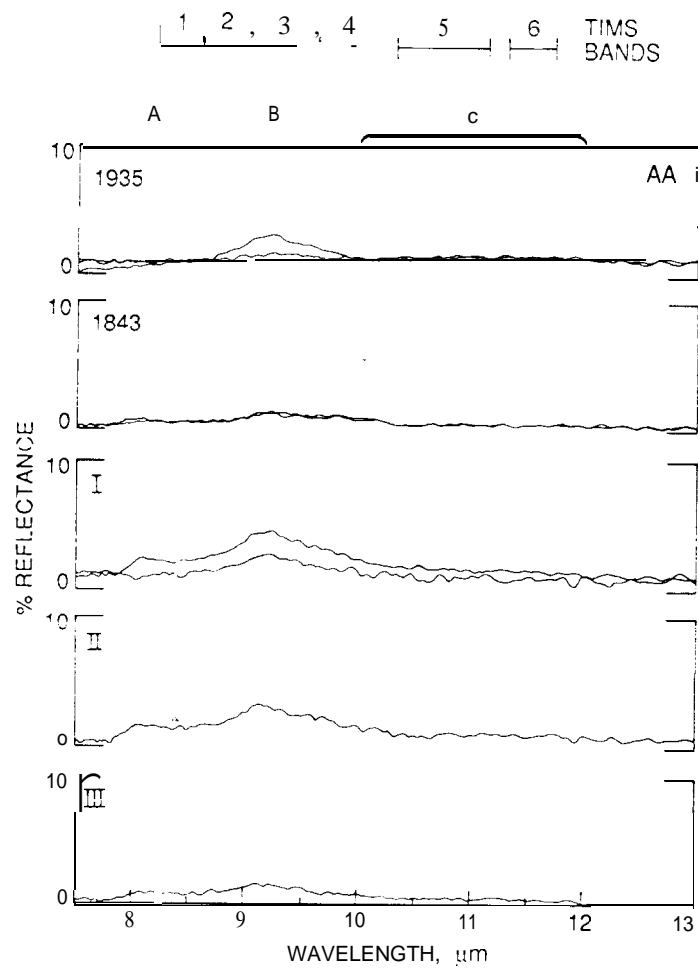
RELATIVE REFLECTANCE (%)

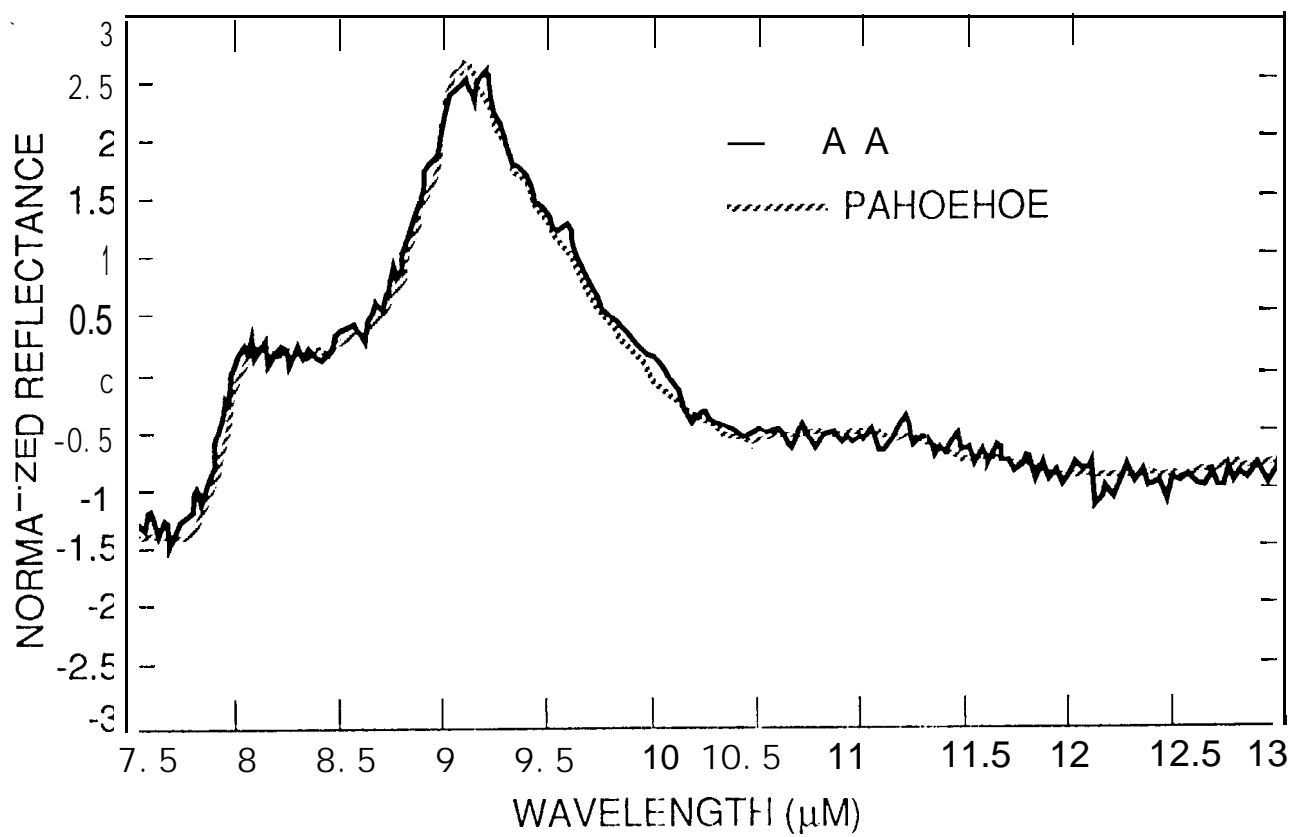


PAHOEHOE

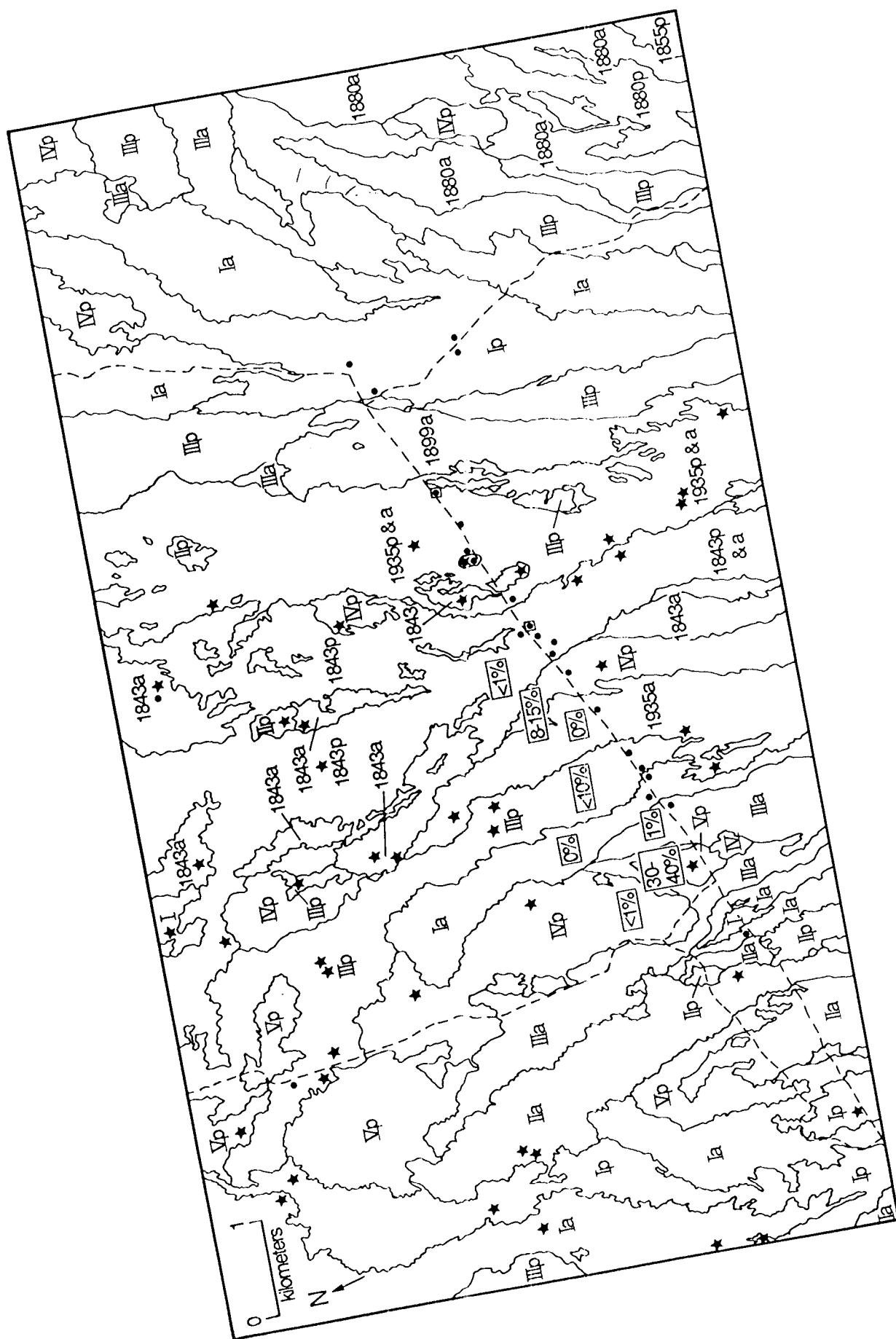
0.4 0.6 0.8 1.0 1.2 1.4 1.6 1.8 2.0 2.2 2.4
WAVELENGTH, μm



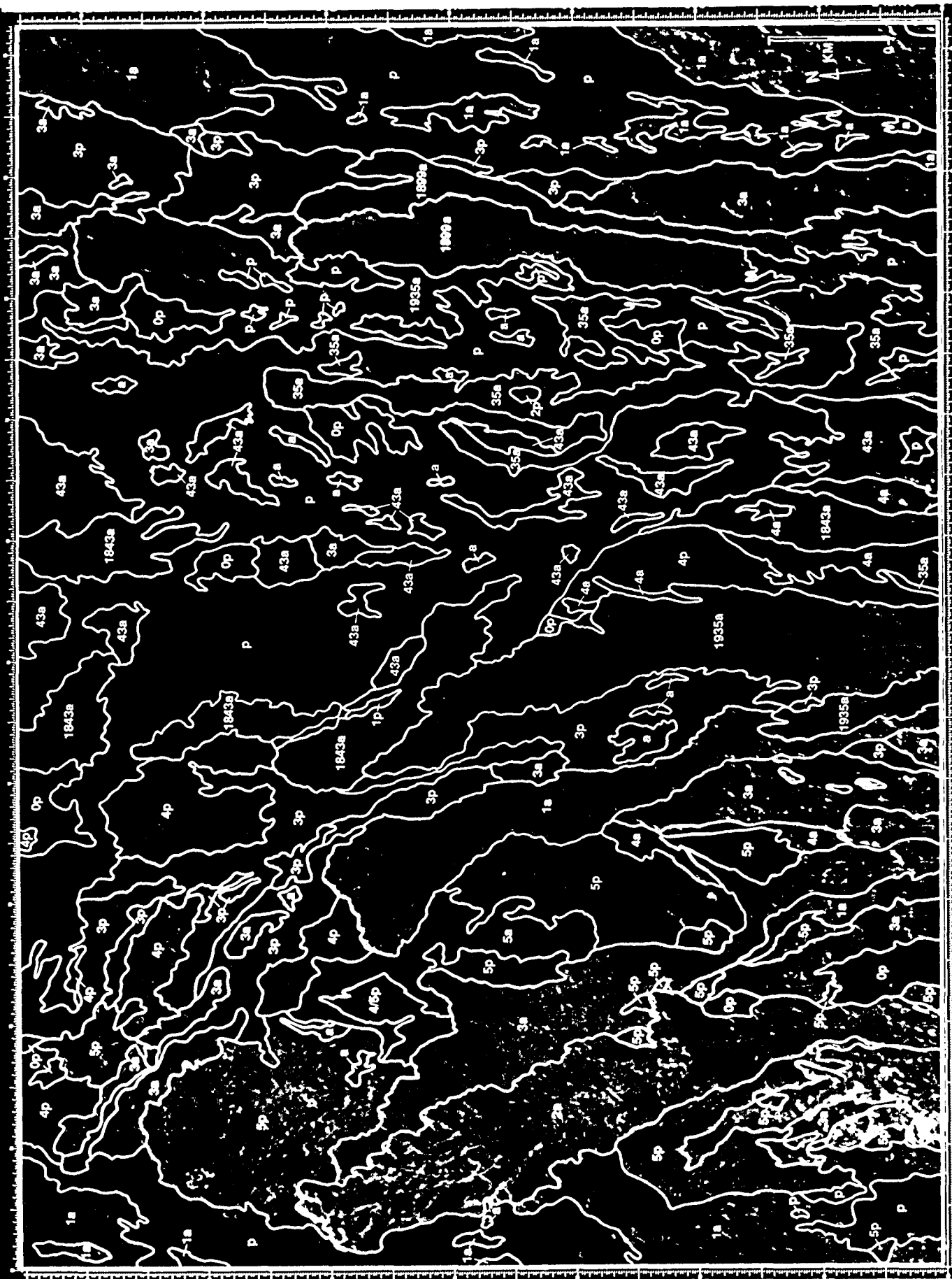




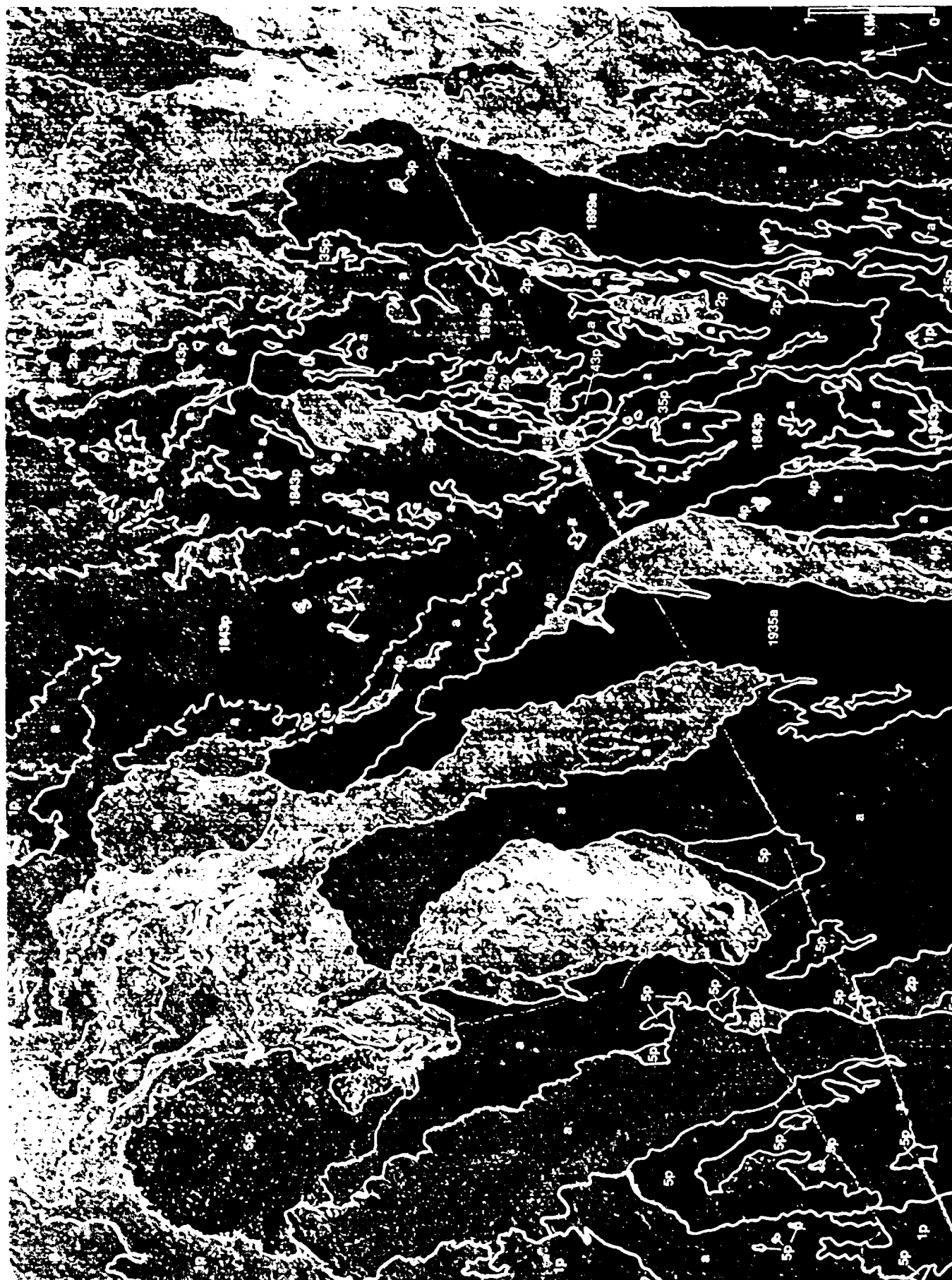




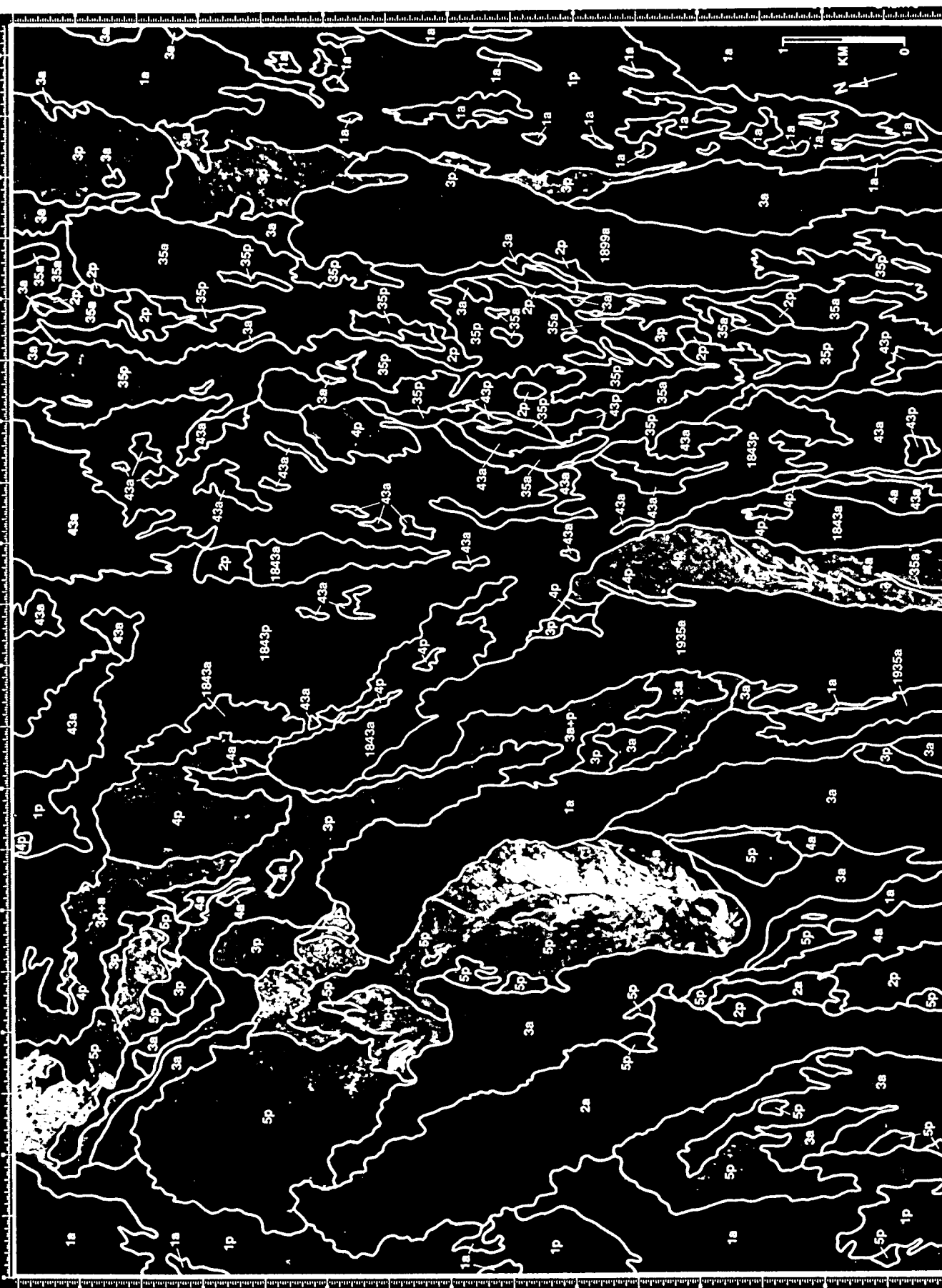
NS-001

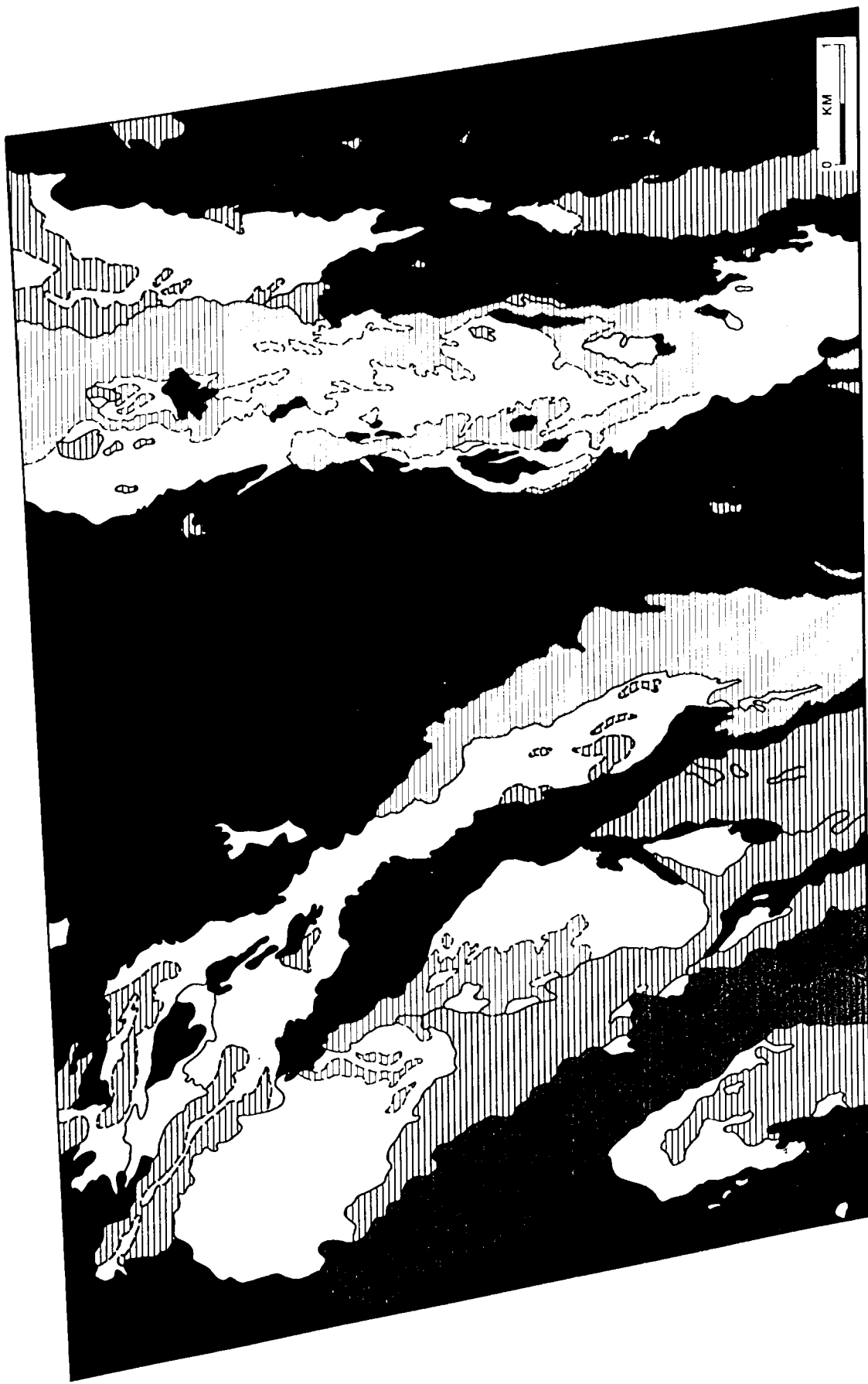


TIMS



TIMS + NS-001





LANDSAT TM TEMPERATURE SENSITIVITIES
(EMISSIVITY = 0.8)

